Supplementary Material

Contents

1 Anomalous Hall effect (AHE) simulation

In the following, the model for the AHE readout is first described. Then, for the geometry of a racetrack, the skyrmion AHE signal is analytically calculated for the case with and without a domain wall, and the case of finite Hall bar contacts is briefly discussed. Afterwards, a numerical method is introduced to verify the analytical calculations, to determine the experimental resistivity tensor, to compute the signal for the exact experimental geometry, and to compare this case with the analytical formulas.

1.1 Model

The coordinate system is defined such that x, y are the in-plane coordinates of the layers, and z denotes the coordinate perpendicular to the layers in the multilayer stack. In the following, we define $\vec{r} = (x, y)$. We assume that the current density $\vec{j}$ is approximately constant along the z-direction and does not vary significantly between the different layers, i.e., $\vec{j} = \vec{j}(x, y)$. Therefore, we model the conductivity tensor $\boldsymbol{\sigma}$ in the multilayer stack as being uniform across all layers, and consequently describe it by an in-plane conductivity tensor $\boldsymbol{\sigma}(x, y)$. The total thickness of all conductive layers is denoted by t. The aim is to solve for the current density within a conductive domain denoted as Ω.

For the conductivity tensor $\boldsymbol{\sigma}$ in the presence of the anomalous Hall effect, the following symmetry relation holds: $\boldsymbol{\sigma}_{xy}(m_z) = \boldsymbol{\sigma}_{yx}(-m_z)$ where $m_z = M_z/M_\mathrm{s}$ is the reduced z-component of the magnetization [1]. Therefore we describe the AHE in terms of the resistivity tensor $\boldsymbol{\rho} = \boldsymbol{\sigma}^{-1}$, which can be expressed as

$$\boldsymbol{\rho} = \begin{pmatrix} \rho_{xx} & \rho_{xy}\, m_z(\vec{r}) \\ -\rho_{xy}\, m_z(\vec{r}) & \rho_{xx} \end{pmatrix}, \tag{S1}$$

under the assumption that the longitudinal resistivity is isotropic, i.e., $\rho_{xx} = \rho_{yy}$. The magnetization component $m_z(\vec{r})$ is position-dependent.

In the following, we consider the current density $\vec{j}(\vec{r},t)$ in the case of equilibrium. Due to charge conservation, the continuity equation $\partial_t \rho + \nabla \cdot \vec{j} = 0$ holds for the current density. In equilibrium, the time derivative vanishes, and we therefore obtain the stationary condition: $\nabla \cdot \vec{j} = 0$. The electric field $\vec{E}$ is related to the current density via Ohm's law $\vec{j} = \boldsymbol{\sigma}\vec{E}$. In the electrostatic case, the electric field can be expressed as the gradient of the scalar electric potential $\varphi(\vec{r})$, i.e., $\vec{E} = -\nabla\varphi$. This leads to the following equation for the electric potential: $0 = \nabla \cdot \vec{j} = -\nabla \cdot (\boldsymbol{\sigma}\nabla\varphi)$, and hence,

$$\nabla \cdot (\boldsymbol{\sigma}\nabla\varphi) = 0, \tag{S2}$$

as also found in the literature [2].

Furthermore, the boundary condition specifies that the normal component of the current density $\vec{j} \cdot \vec{n}$ at the boundary is known, where $\vec{n}$ denotes the outward-pointing unit normal vector at the boundary. This results in a Neumann boundary condition for the potential φ:

$$-(\boldsymbol{\sigma}\ \nabla\varphi|_{\vec{r}}) \cdot \vec{n} = j(\vec{r}) \quad \text{for } \vec{r} \in \partial\Omega, \tag{S3}$$

where $\partial\Omega$ is the boundary edge with outward normal vector $\vec{n}$, and $j(\vec{r})$ denotes the current density component flowing perpendicular to the boundary.

1.2 Analytical solution

1.2.1 Analytical formalism for AHE signals

In the following, a small anomalous Hall angle $\theta = \rho_{xy}/\rho_{xx}$ is assumed, i.e., $|\theta| \ll 1$, which is the case for our system and for a wide range of magnetic materials. As shown in the following steps, it is required to solve the Laplace equation for the considered domain Ω. Since solving the Laplace equation analytically with the appropriate boundary conditions is very complicated for arbitrary domains Ω, we therefore consider a racetrack-shaped (rectangular) domain in which the current flows along the x-direction. The choice of the x-direction is, of course, made without loss of generality. This racetrack has a length L in the x-direction and a width W in the y-direction, where the length L is much greater than the spatial extent of the considered domain for which the AHE signal is calculated. Therefore, we consider, in the limit $L \to \infty$,

$$\Omega = \left\{(x,y) \in \mathbb{R}^2 \middle| -L/2 \le x \le L/2, -W/2 \le y \le W/2\right\}, \tag{S4}$$

where a current density j is injected along the x-direction, leading to the following boundary conditions:

$$-\left(\boldsymbol{\rho}^{-1}\nabla\varphi\big|_{x=\pm L/2}\right) \cdot \vec{e}_x = j \quad \text{and} \quad \left(\boldsymbol{\rho}^{-1}\nabla\varphi\big|_{y=\pm W/2}\right) \cdot \vec{e}_y = 0. \tag{S5}$$

This rectangular domain is also a good approximation for the case where the racetrack has Hall contacts, as long as the Hall contacts are small compared to the magnetic structure and the width of the racetrack.

To solve the partial differential equation, the first step is to simplify it using perturbation theory. We make the ansatz for the solution of the differential equation $\varphi = \phi_0 + \theta\phi_1$, where ϕ_0 is the solution of the equation without the anomalous Hall effect, and ϕ_1 represents the first-order correction due to the anomalous Hall effect. We consider only linear perturbations in terms of θ. In this case, $\boldsymbol{\rho}^{-1}$ is given by

$$\boldsymbol{\rho}^{-1} = \rho_{xx}^{-1} \begin{pmatrix} 1 & -\theta\, m_z(\vec{r}) \\ \theta\, m_z(\vec{r}) & 1 \end{pmatrix}, \tag{S6}$$

since $\rho_{xx}^2 + \rho_{xy}^2 = \rho_{xx}^2(1+\theta^2) \approx \rho_{xx}^2 + \mathcal{O}(\theta^2)$. Substituting the ansatz into Equation S2, we obtain

$$\Delta\phi_0 + \theta(\Delta\phi_1 + \ \partial_y m_z \partial_x \phi_0 - \partial_x m_z \partial_y \phi_0) + \theta^2 \left(\partial_y m_z \partial_x \phi_1 - \partial_x m_z \partial_y \phi_1\right) = 0. \tag{S7}$$

Since this equation must hold for all sufficiently small values of θ, we can compare coefficients of equal powers of θ. This step is valid because the equation holds for all small values of θ, which means that the coefficients of each power of θ must vanish separately. Neglecting terms of order $\mathcal{O}(\theta^2)$, one obtains

$$\Delta\phi_0 = 0 \quad \text{and} \quad \Delta\phi_1 = \partial_x m_z \partial_y \phi_0 - \partial_y m_z \partial_x \phi_0. \tag{S8}$$

Thus, the problem reduces to solving a Poisson equation for ϕ_1. In the absence of the anomalous Hall effect, this leads to the term $\Delta\phi_0 = 0$ – the Laplace equation – since ϕ_0 represents the electric potential without the anomalous Hall effect, where there are no internal sources of the electric field within the considered domain Ω. The potential ϕ_0 is determined solely by the external current flowing into and out of the domain, as specified by the boundary conditions. The function ϕ_1 then provides the additional contribution due to the anomalous Hall effect, with the corresponding source term given by $\partial_x m_z\, \partial_y \phi_0 - \partial_y m_z\, \partial_x \phi_0$. This term represents the spatial variation of the z-component of the magnetization $\vec{m}$ combined with the spatial derivatives of the local potential ϕ_0 in the absence of the anomalous Hall effect.

In the first step, ϕ_0 (the contribution for $\theta = 0$) is determined from the boundary conditions given in Equation S5 for $\theta = 0$. For the rectangular geometry, the solution of $\Delta\phi_0 = 0$ is

$$\phi_0 = -j\,\rho_{xx}\,x. \tag{S9}$$

To solve for ϕ_1, it is decomposed into $\phi_1 = \phi_{1,\mathrm{p}} + \phi_{1,\mathrm{h}}$, where $\phi_{1,\mathrm{p}}$ denotes the particular solution, which is determined for the infinite two-dimensional plane $\mathbb{R}^2$, i.e., without considering boundary conditions, and $\phi_{1,\mathrm{h}}$ denotes the homogeneous solution, which incorporates the boundary conditions for the finite domain Ω. The particular solution $\phi_{1,\mathrm{p}}$ is obtained via the Green's function G. For $\mathbb{R}^2$, the Green's function satisfies $\Delta_{\vec{r}} G(\vec{r}, \vec{r}') = \delta(\vec{r} - \vec{r}')$, with the solution given by $G(\vec{r}, \vec{r}') = \frac{1}{2\pi}\log(|\vec{r} - \vec{r}'|)$. This leads to

$$\phi_{1,\mathrm{p}}(\vec{r}') = \int \mathrm{d}^2\vec{r}\, G(\vec{r}', \vec{r})(\partial_x m_z(\vec{r})\partial_y\phi_0(\vec{r}) - \partial_y m_z(\vec{r})\partial_x\phi_0(\vec{r})). \tag{S10}$$

Using Equation S9, this expression simplifies to

$$\phi_{1,\mathrm{p}}(\vec{r}') = \frac{j\rho_{xx}}{2\pi}\int \mathrm{d}^2\vec{r}\,\log(|\vec{r} - \vec{r}'|)\,\partial_y m_z(\vec{r}). \tag{S11}$$

Next, the homogeneous equation for $\phi_{1,\mathrm{h}}$ must be solved, subject to $\Delta\phi_{1,\mathrm{h}} = 0$ and the boundary conditions, such that the total potential $\varphi = \phi_0 + \theta\,(\phi_{1,\mathrm{h}} + \phi_{1,\mathrm{p}})$ satisfies the boundary conditions given in Equation S5, with $\boldsymbol{\rho}^{-1}$ defined by Equation S6. This leads to

$$(\theta\partial_x\phi_1 - \theta^2\, m_z(\vec{r})\partial_y\phi_1)\big|_{x=\pm L/2} = 0 \quad \text{and} \quad ((-j\rho_{xy} + \theta^2\partial_x\phi_1)\, m_z(\vec{r}) + \theta\partial_y\phi_1)\big|_{y=\pm W/2} = 0. \tag{S12}$$

Neglecting terms of order θ^2, the boundary condition for $\phi_{1,\mathrm{h}}$ is obtained as

$$\partial_x\phi_1|_{x=\pm L/2} = 0 \quad \text{and} \quad \partial_y\phi_{1,\mathrm{h}}|_{y=\pm W/2} = -\,\partial_y\phi_{1,\mathrm{p}}|_{y=\pm W/2} + j\rho_{xx}\, m_z(x, y = \pm W/2). \tag{S13}$$

The nontrivial part of the homogeneous solution $\phi_{1,\mathrm{h}}$ is obtained by separation of variables, $\phi_{1,\mathrm{h}} = \phi_{1,x}(x)\,\phi_{1,y}(y)$, in addition to the trivial solution $C_0 + C_x x + C_y y + C_{xy} xy$. Applying the boundary condition $\partial_x\phi_{1,\mathrm{h}}|_{x=\pm L/2} = 0$ yields

$$\begin{aligned}\phi_{1,\mathrm{h}} = C_y y + \sum_{n=1}^{\infty} &\left(a_k \exp\left(\frac{2\pi n}{L}y\right) + b_k \exp\left(-\frac{2\pi n}{L}y\right)\right)\cos\left(\frac{2\pi n}{L}x\right) \\ &+ \left(c_k \exp\left(\frac{2\pi n}{L}y\right) + d_k \exp\left(-\frac{2\pi n}{L}y\right)\right)\sin\left(\frac{\pi(2n+1)}{L}x\right),\end{aligned} \tag{S14}$$

where $C_y, a_k, b_k, c_k, d_k \in \mathbb{R}$. Since the limit $L \to \infty$ is considered, the solution simplifies to

$$\begin{aligned}\phi_{1,\mathrm{h}} &= C_y y + \int_0^{\infty} \mathrm{d}k\ (a(k)\exp(ky) + b(k)\exp(-ky))\cos(kx) + (c(k)\exp(ky) + d(k)\exp(-ky))\sin(kx), \\ &= C_y y + \int_{-\infty}^{\infty} \mathrm{d}k\ \left(\tilde{a}(k)\exp(ky) + \tilde{b}(k)\exp(-ky)\right)\exp(ikx),\end{aligned} \tag{S15}$$

with complex coefficients $\tilde{a}(k), \tilde{b}(k) \in \mathbb{C}$. The boundary condition at the top and bottom edges, $\partial_y\phi_{1,\mathrm{h}}|_{y=\pm W/2}$, must also be satisfied. Since, for $|x| \to \infty$, the derivative of the particular solution $\partial_y\phi_{1,\mathrm{p}}|_{y=\pm W/2}$ vanishes, only the term $+j\rho_{xx}\, m_z(x \to \infty, y = \pm W/2)$ remains, where $m_z(x \to \infty, y = \pm W/2)$ corresponds to the ferromagnetic background magnetization $m_{z,\mathrm{B}}$. Therefore, the coefficient

C_y is set to $C_y = j\rho_{xx} m_{z,\mathrm{B}}$. With this, the oefficients $\tilde{a}(k)$ and $\tilde{b}(k)$ can be determined by comparing the boundary conditions with the general solution for $\phi_{1,\mathrm{h}}$, i.e.,

$$\begin{aligned} B_{\pm W/2}(x) &= -\,\partial_y \phi_{1,\mathrm{p}}|_{y=\pm W/2} + j\rho_{xx}\left(m_z(x, y=\pm W/2) - m_{z,\mathrm{B}}\right) \\ &= \int_{-\infty}^{\infty} \mathrm{d}k \,\left(k\tilde{a}(k)\exp\left(\pm W/2\right) - k\tilde{b}(k)\exp\left(\mp W/2\right)\right)\exp(ikx), \end{aligned} \tag{S16}$$

where $B_{\pm W/2}(x)$ denotes the derivative of the homogeneous solution at the boundary, shifted by $-j\rho_{xx} m_{z,\mathrm{B}}$. Using the inverse Fourier transformation and some algebraic simplification, the homogeneous part $\phi_{1,\mathrm{h}}$ is then given by

$$\phi_{1,\mathrm{h}}(x,y) = j\rho_{xx} m_{z,\mathrm{B}} y + \int_{-\infty}^{\infty} \mathrm{d}k \,\frac{\hat{B}_{+W/2}(k)\cosh\left(\frac{1}{2}k(W+2y)\right) - \hat{B}_{-W/2}(k)\cosh\left(\frac{1}{2}k(W-2y)\right)}{k\sinh(kW)}\,\exp(ikx) \tag{S17}$$

where $\hat{B}_{\pm W/2}(k)$ denotes the Fourier transform of $B_{\pm W/2}(x)$ with respect to the x-coordinate, i.e.,

$$\hat{B}_{\pm W/2}(k) = \frac{1}{2\pi}\int_{-\infty}^{\infty} B_{\pm W/2}(x)\exp(-ikx). \tag{S18}$$

In the symmetric case, where the boundary conditions at the top and bottom edges are identical, i.e., $B_{+W/2}(x) = B_{-W/2}(x)$, it follows that $\hat{B}_{+W/2}(k) = \hat{B}_{-W/2}(k)$, and the expression for $\phi_{1,\mathrm{h}}$ simplifies to

$$\phi_{1,\mathrm{h}}(x,y) = j\rho_{xx} m_{z,\mathrm{B}} y + \int_{-\infty}^{\infty} \mathrm{d}k\, \hat{B}_{+W/2}(k)\frac{\sinh(ky)}{k\cosh(kW/2)}\,\exp(ikx). \tag{S19}$$

For a given magnetization profile $m_z(\vec{r})$, the solution is therefore explicitly determined by the preceding expressions together with the definition of the electric potential $\varphi = \phi_0 + \theta\,(\phi_{1,\mathrm{p}} + \phi_{1,\mathrm{h}})$. The AHE signal R_{xy}, corresponding to the potential difference measured between the top and bottom edges at $y = \pm W/2$, is given by

$$R_{xy}(x) = \frac{V_y}{I_x} = \frac{V_y}{jWt} = \frac{\varphi(x, W/2) - \varphi(x, -W/2)}{jWt} = \theta\frac{(\phi_{1,\mathrm{p}} + \phi_{1,\mathrm{h}})(x, W/2) - (\phi_{1,\mathrm{p}} + \phi_{1,\mathrm{h}})(x, -W/2)}{jWt}. \tag{S20}$$

Since $\phi_{1,\mathrm{p}} + \phi_{1,\mathrm{h}} \propto j\rho_{xx}$, it follows directly that $R_{xy} \propto \frac{\theta\rho_{xx}}{t} = \frac{\rho_{xy}}{t}$.

Since the calculation of R_{xy} requires the potential difference of the homogeneous solution, the expression of Equation S17 can be simplified to

$$\phi_{1,\mathrm{h}}(x, W/2) - \phi_{1,\mathrm{h}}(x, -W/2) = j\rho_{xx} m_{z,\mathrm{B}} W + \int_{-\infty}^{\infty} \mathrm{d}k\,(\hat{B}_{+W/2}(k) + \hat{B}_{-W/2}(k))\frac{1}{k}\tanh\left(\frac{kW}{2}\right)\exp(ikx). \tag{S21}$$

Note that for $m_z = \text{const.} = m_{z,\mathrm{B}}$ in the rectangular domain $[-L/2, L/2] \times [-W/2, W/2]$, and without any further assumptions or the use of perturbation theory, the solution is given by,

$$\varphi = j(-\rho_{xx} x + m_{z,\mathrm{B}}\rho_{xy} y) \tag{S22}$$

since

$$\boldsymbol{\rho}^{-1}\nabla\varphi = \frac{j}{\rho_{xx}^2 + \rho_{xy}^2 m_{z,\mathrm{B}}^2}\begin{pmatrix}\rho_{xx} & -\rho_{xy} m_{z,\mathrm{B}} \\ \rho_{xy} m_{z,\mathrm{B}} & \rho_{xx}\end{pmatrix}\begin{pmatrix}-\rho_{xx} \\ m_{z,\mathrm{B}}\rho_{xy}\end{pmatrix} = \begin{pmatrix}-j \\ 0,\end{pmatrix} \tag{S23}$$

and therefore satisfies Equation S2 and Equation S5. This result is consistent with the expressions derived by perturbation theory for $m_z = \text{const.} = m_{z,\mathrm{B}}$, since in this case $\phi_0 = -j\rho_{xx} x$, $\phi_{1,\mathrm{p}} = 0$, and $\phi_{1,\mathrm{h}} = j\rho_{xx} m_{z,\mathrm{B}} y$. Hence, the total potential $\varphi = \phi_0 + \theta(\phi_{1,\mathrm{p}} + \phi_{1,\mathrm{h}}) = j(-\rho_{xx} x + \rho_{xy} m_{z,\mathrm{B}} y)$, which reproduces the exact same result.

1.2.2 Skyrmion with negligible domain wall width

With this formalism, the signal for a skyrmion of radius R_{S}, whose domain-wall width can be neglected, placed at position $(x_{\mathrm{S}}, y_{\mathrm{S}})$ inside the racetrack, can now be calculated, i.e.,

$$m_z(x,y) = \begin{cases} m_{z,\mathrm{S}} & (x-x_{\mathrm{S}})^2 + (x-y_{\mathrm{S}})^2 < R_{\mathrm{S}}^2 \\ m_{z,\mathrm{B}} & \text{otherwise}\end{cases} = (m_{z,\mathrm{S}} - m_{z,\mathrm{B}})H(R_{\mathrm{S}} - r) + m_{z,\mathrm{B}}, \tag{S24}$$

where H denotes the Heaviside step function, r is the radial distance, and α is the polar angle measured with respect to the skyrmion center at $(x_\mathrm{S}, y_\mathrm{S})$, i.e., $\vec{r} = (x_\mathrm{S} + r\cos\alpha)\,\vec{e}_x + (y_\mathrm{S} + r\sin\alpha)\,\vec{e}_y$. We consider the case $2R_\mathrm{S} \leq W$, so that the maximum skyrmion diameter does not exceed the racetrack width W. Typically, $m_{z,\mathrm{B}} = -m_{z,\mathrm{S}} = 1$ or $m_{z,\mathrm{B}} = -m_{z,\mathrm{S}} = -1$, but $m_{z,\mathrm{B}}$ and $m_{z,\mathrm{S}}$ are treated as independent parameters in the following discussion for later use.

First, the particular solution from Equation S11 is calculated for the electric field of a skyrmion in $\mathbb{R}^2$. For this purpose, the derivative $\partial_y m_z$ is given by $(\partial_y m_z)(r) = \sin(\alpha)\,\partial_r m_z(r)$ (for any skyrmion with a radially symmetric profile). With this, the particular solution is given by

$$\begin{aligned}
\phi_{1,\mathrm{p}}(r,\alpha) &= \frac{j\rho_{xx}}{4\pi}\int_0^\infty \mathrm{d}r'\, r'\partial_{r'}m_z(r')\int_0^{2\pi}\mathrm{d}\alpha'\,\log(r^2+r'^2-2rr'\cos(\alpha-\alpha'))\sin(\alpha') \\
&= \frac{j\rho_{xx}}{4\pi}\int_0^\infty \mathrm{d}r'\, r'\partial_{r'}m_z(r')\int_0^{2\pi}\mathrm{d}\alpha'\,\log\left(1-\frac{2rr'}{r^2+r'^2}\cos(\alpha-\alpha')\right)\sin(\alpha') \\
&= \frac{j\rho_{xx}\sin(\alpha)}{2}\int_0^\infty \mathrm{d}r'\, r'\partial_{r'}m_z(r')\left[\sqrt{\left(\frac{r^2+r'^2}{2rr'}\right)^2-1}-\frac{r^2+r'^2}{2rr'}\right] \\
&= \frac{j\rho_{xx}\sin(\alpha)}{4}\int_0^\infty \mathrm{d}r'\,\partial_{r'}m_z(r')\frac{1}{r}\left[\left|r^2-r'^2\right|-r^2-r'^2\right] \\
&= -\frac{j\rho_{xx}\sin(\alpha)}{2}\int_0^\infty \mathrm{d}r'\,\partial_{r'}m_z(r')\begin{cases} r, & r\leq r', \\ \frac{r'^2}{r}, & r\geq r'. \end{cases}
\end{aligned} \tag{S25}$$

In these steps, only the radial symmetry of the skyrmion has been used. Now, using Equation S24, one obtains $\partial_{r'}m_z(r') = (m_{z,\mathrm{B}} - m_{z,\mathrm{S}})\,\delta(R_\mathrm{S} - r')$, so that $\phi_{1,\mathrm{p}}(r,\alpha)$ simplifies to

$$\begin{aligned}
\phi_{1,\mathrm{p}}(x,y) = \phi_{1,\mathrm{p}}(r,\alpha) &= -\frac{m_{z,\mathrm{B}}-m_{z,\mathrm{S}}}{2}j\rho_{xx}\sin(\alpha)r\begin{cases}1, & r<R_\mathrm{S}, \\ \frac{R_\mathrm{S}^2}{r^2}, & r>R_\mathrm{S},\end{cases} \\
&= -\frac{m_{z,\mathrm{B}}-m_{z,\mathrm{S}}}{2}j\rho_{xx}(y-y_\mathrm{S})\begin{cases}1, & \text{if } (x-x_\mathrm{S})^2+(y-y_\mathrm{S})^2<R_\mathrm{S}^2, \\ \frac{R_\mathrm{S}^2}{(x-x_\mathrm{S})^2+(y-y_\mathrm{S})^2}, & \text{otherwise.}\end{cases}
\end{aligned} \tag{S26}$$

This result provides the electric potential $\varphi = \phi_0 + \theta\,\phi_{1,\mathrm{p}}$ for a skyrmion in an infinitely extended magnetic film in both the x and y directions, arising from the anomalous Hall effect.

Based on this, the homogeneous contribution to the electric field can be calculated. To simplify the computation, the potential difference $\phi_{1,\mathrm{h}}(x,-W/2) - \phi_{1,\mathrm{h}}(x,+W/2)$ is evaluated directly using Equation S21. For this purpose, $\hat{B}_{\pm W/2}(k)$ must be determined from $B_{\pm W/2}(x)$. The function $B_{\pm W/2}(x)$, defined in Equation S16, is given by

$$B_{\pm W/2}(x) = -\,\partial_y\phi_{1,\mathrm{p}}|_{y=\pm W/2} = \frac{m_{z,\mathrm{B}}-m_{z,\mathrm{S}}}{2}j\rho_{xx}R_\mathrm{S}^2\frac{(x-x_\mathrm{S})^2-(\pm W/2-y_\mathrm{S})^2}{((x-x_\mathrm{S})^2+(\pm W/2-y_\mathrm{S})^2)^2} \tag{S27}$$

since $R_\mathrm{S} \leq W/2$. For the function $h(x) = \dfrac{x^2-y^2}{(x^2+y^2)^2}$ with $y>0$, the corresponding Fourier transform is given by

$$\hat{h}(k) = \frac{1}{2\pi}\int_{-\infty}^{\infty}\mathrm{d}x\,\frac{x^2-y^2}{(x^2+y^2)^2}\exp(-ikx) = \frac{k}{2}\begin{cases}-\exp(-ky), & k\geq 0, \\ \exp(ky), & k\leq 0.\end{cases} \tag{S28}$$

Using this result, the Fourier transform of $B_{\pm W/2}(x)$ can be expressed as

$$B_{\pm W/2}(k) = \frac{m_{z,\mathrm{B}}-m_{z,\mathrm{S}}}{2}j\,\rho_{xx}R_\mathrm{S}^2\exp(-ikx_\mathrm{S})\frac{k}{2}\begin{cases}-\exp(-k|\pm W/2-y_\mathrm{S}|), & k\geq 0, \\ \exp(k|\pm W/2-y_\mathrm{S}|), & k\leq 0,\end{cases} \tag{S29}$$

and consequently, the potential difference of the harmonic contribution becomes

$$\phi_{1,\mathrm{h}}(x,-W/2)-\phi_{1,\mathrm{h}}(x,+W/2) = j\rho_{xx}m_{z,\mathrm{B}}W - 2(m_{z,\mathrm{B}}-m_{z,\mathrm{S}})j\rho_{xx}R_\mathrm{S}^2\int_0^\infty \mathrm{d}k\,\frac{\cosh(ky_\mathrm{s})\sinh\left(\frac{kW}{2}\right)}{1+\exp(kW)}\cos(k(x-x_\mathrm{S})). \tag{S30}$$

Since

$$\int_0^\infty \mathrm{d}k \frac{e^{-ak+ibk(x-x_\mathrm{S})}}{e^{kW}+1} = \frac{1}{2W}\left[\psi\left(\frac{a+2W-ib\,(x-x_\mathrm{S})}{2W}\right) - \psi\left(\frac{a+W-ib\,(x-x_\mathrm{S})}{2W}\right)\right], \tag{S31}$$

where ψ denotes the digamma function, the integral determining the potential difference of the harmonic component can be evaluated analytically. After some algebraic manipulation and simplification, the final result reads

$$\begin{aligned}\phi_{1,\mathrm{h}}(x,W/2) - \phi_{1,\mathrm{h}}(x,-W/2) &= +j\rho_{xx} m_{z,\mathrm{B}} W \\ + j\rho_{xx} R_\mathrm{S}^2 \frac{m_{z,\mathrm{B}} - m_{z,\mathrm{S}}}{2} &\left[\frac{W/2-y_\mathrm{S}}{(x-x_\mathrm{S})^2+(W/2-y_\mathrm{S})^2} + \frac{W/2+y_\mathrm{S}}{(x-x_\mathrm{S})^2+(W/2+y_\mathrm{S})^2} - \frac{4\pi}{W}\frac{\cos\left(\frac{\pi y_\mathrm{S}}{W}\right)\cosh\left(\frac{\pi(x-x_\mathrm{S})}{W}\right)}{\cos\left(\frac{2\pi y_\mathrm{S}}{W}\right)+\cosh\left(\frac{2\pi(x-x_\mathrm{S})}{W}\right)}\right].\end{aligned} \tag{S32}$$

By combining the particular and homogeneous solutions, the anomalous Hall effect signal of the electric potential φ can be obtained. According to Equation S20, this yields

$$R_{xy}(x_\mathrm{S},y_\mathrm{S}) = \frac{\varphi(x,W/2)-\varphi(x,-W/2)}{jWt} = \frac{\rho_{xy}}{t}\left(m_{z,\mathrm{B}} - (m_{z,\mathrm{B}}-m_{z,\mathrm{S}})2\pi\left(\frac{R_\mathrm{S}}{W}\right)^2 \frac{\cos\left(\frac{\pi y_\mathrm{S}}{W}\right)\cosh\left(\frac{\pi(x-x_\mathrm{S})}{W}\right)}{\cos\left(\frac{2\pi y_\mathrm{S}}{W}\right)+\cosh\left(\frac{2\pi(x-x_\mathrm{S})}{W}\right)}\right). \tag{S33}$$

It provides the Hall signal $R_{xy}(x)$ for a skyrmion located at $(x_\mathrm{S}, y_\mathrm{S})$ with radius R_S, where typically $m_{z,\mathrm{S}} = -m_{z,\mathrm{B}} = -1$. In this case, the expression simplifies to

$$R_{xy}(x_\mathrm{S},y_\mathrm{S}) = \frac{\rho_{xy}}{t}\left(1 - 4\pi\left(\frac{R_\mathrm{S}}{W}\right)^2 \frac{\cos\left(\frac{\pi y_\mathrm{S}}{W}\right)\cosh\left(\frac{\pi(x-x_\mathrm{S})}{W}\right)}{\cos\left(\frac{2\pi y_\mathrm{S}}{W}\right)+\cosh\left(\frac{2\pi(x-x_\mathrm{S})}{W}\right)}\right). \tag{S34}$$

1.2.3 Skyrmion with finite domain wall width

Next, the solution for a general radially symmetric skyrmion is considered, i.e., the skyrmion profile is given by $m_z(r)$, where r denotes the distance from the skyrmion center and α is the polar angle measured from the origin $(x_\mathrm{S}, y_\mathrm{S})$. In polar coordinates, this can be written as $\vec{r} = (x_\mathrm{S} + r\cos\alpha)\,\vec{e}_x + (y_\mathrm{S} + r\sin\alpha)\,\vec{e}_y$. Consider again Equation S8,

$$\Delta\phi_1 = j\rho_{xx}\partial_y m_z = j\rho_{xx}\sin(\alpha)\partial_r m_z, \tag{S35}$$

which must be solved with the boundary conditions given in Equation S5. One therefore defines a modified Green's function $G_\mathrm{S}(\vec{r}, r')$ satisfying

$$\Delta_{\vec{r}} G_\mathrm{S}(\vec{r},r') = j\rho_{xx}\sin(\alpha)\delta(|\vec{r}|-r'), \tag{S36}$$

with the boundary condition

$$\partial_x G_\mathrm{S}|_{x=\pm L/2} = 0 \quad \text{and} \quad \partial_y G_\mathrm{S}|_{y=\pm W/2} = 0. \tag{S37}$$

From this, the particular solution can be constructed as

$$\phi_{1,\mathrm{p}}(\vec{r}) = \int_0^\infty \mathrm{d}r'\, G_\mathrm{S}(\vec{r},r')\partial_{r'} m_z(r'), \tag{S38}$$

which satisfies Equation S35. Additionally, the homogeneous solution $\phi_{1,\mathrm{h}}$ is given by Equation S17, where $\hat{B}_{\pm W/2}(k)$ is defined in Equation S18, but $B_{\pm W/2}(x)$ is now given by

$$B_{\pm W/2}(x) = j\rho_{xx}\,(m_z(x, y=\pm W/2) - m_{z,\mathrm{B}}). \tag{S39}$$

The total potential $\varphi = \phi_0 + \theta\,(\phi_{1,\mathrm{p}} + \phi_{1,\mathrm{h}})$, thus satisfies the original partial differential equation Equation S8 and the boundary conditions Equation S5.

The problem is now reformulated, with the key objective being the determination of the modified Green's function $G_{\mathrm{S}}(\vec{r}, r')$. For the case in which the circle centered at $(x_{\mathrm{S}}, y_{\mathrm{S}})$ does not intersect the boundary, i.e.,

$$r' < \min(W/2 - y_{\mathrm{S}}, W/2 + y_{\mathrm{S}}) = r_{\mathrm{c}}, \tag{S40}$$

the following difference of the modified Green's function at two points was implicitly obtained in the previous section:

$$\begin{aligned}
\Delta G(x, r') &= G_{\mathrm{S}}(\vec{r} = (x, W/2), r') - G_{\mathrm{S}}(\vec{r} = (x, -W/2), r') \\
&= \phi_{1,\mathrm{p}}(x, W/2) - \phi_{1,\mathrm{p}}(x, -W/2) + \phi_{1,\mathrm{h}}(x, W/2) - \phi_{1,\mathrm{h}}(x, -W/2) \\
&= -j\rho_{xx} \frac{2\pi r'^2}{W} \frac{\cos\left(\frac{\pi y_{\mathrm{S}}}{W}\right) \cosh\left(\frac{\pi(x - x_{\mathrm{S}})}{W}\right)}{\cos\left(\frac{2\pi y_{\mathrm{S}}}{W}\right) + \cosh\left(\frac{2\pi(x - x_{\mathrm{S}})}{W}\right)}.
\end{aligned} \tag{S41}$$

In this equation, the functions $\phi_{1,\mathrm{h}}$ and $\phi_{1,\mathrm{p}}$ are defined according to the expressions introduced in subsubsection 1.2.2, with $m_{z,\mathrm{B}} = 0$ and $m_{z,\mathrm{S}} = -1$. Since only the potential difference at the boundary is required, and by using Equation S38, it follows that ΔG represents the only relevant quantity for which G_{S} must be evaluated. Moreover, because G_{S} is used exclusively in Equation S38, and given that $\partial_r m_z(r) \approx 0$ for $r \geq r_{\mathrm{c}}$, since for a skyrmion confined within a racetrack the magnetization at the boundary should correspond to the ferromagnetic background, and the magnetization associated with the skyrmion therefore remains approximately constant, Equation S41 can be used as an accurate approximation for all r. Furthermore, for $B_{\pm W/2}$, as defined in Equation S39, a similar approximation is applied–namely, that the magnetization at the boundary equals the background magnetization–leading to $B_{\pm W/2} = 0$. From this, it follows that the homogeneous solution is $\phi_{1,\mathrm{h}} = j\rho_{xx} m_{z,\mathrm{B}} y$. Using $\varphi = \phi_0 + \theta(\phi_{1,\mathrm{p}} + \phi_{1,\mathrm{h}})$, the potential difference defined in Equation S20 becomes

$$\begin{aligned}
R_{xy} &= \frac{\varphi(x, W/2) - \varphi(x, -W/2)}{jWt} \\
&= \frac{\rho_{xy} m_{z,\mathrm{B}}}{t} + \theta \int_0^\infty \mathrm{d}r' \, \Delta G(x, r') \, \partial_{r'} m_z(r') \\
&= \frac{\rho_{xy} m_{z,\mathrm{B}}}{t} \left(1 - 4\frac{\mathcal{A}}{W^2} \frac{\cos\left(\frac{\pi y_{\mathrm{S}}}{W}\right) \cosh\left(\frac{\pi(x - x_{\mathrm{S}})}{W}\right)}{\cosh\left(\frac{2\pi(x - x_{\mathrm{S}})}{W}\right) + \cos\left(\frac{2\pi y_{\mathrm{S}}}{W}\right)}\right)
\end{aligned} \tag{S42}$$

where $\mathcal{A}$ is defined as

$$\mathcal{A} = \frac{\pi}{2\, m_{z,\mathrm{B}}} \int_0^\infty \mathrm{d}r \, r^2 \, \partial_r m_z(r) = \frac{\pi}{m_{z,\mathrm{B}}} \int_0^\infty \mathrm{d}r \, r \, (m_{z,\mathrm{B}} - m_z(r)) \tag{S43}$$

where, in the second step, partial integration was applied. Therefore, $\mathcal{A}$ is the effective area parameter that encapsulates the part of the skyrmion structure determining the AHE signal.

For the previously considered case of a negligible domain wall, leading to the same result as before is obtained, leading to Equation S33. Specifically, for case $m_{z,\mathrm{B}} = -m_{z,\mathrm{S}}$, it follows that $\mathcal{A} = \pi R_{\mathrm{S}}^2$.

To obtain a concrete expression for the signal, the well-established skyrmion profile ansatz from Ref. [3] is adopted:

$$\begin{aligned}
m_z(r) &= -m_{z,\mathrm{B}} \cos\left(\arcsin(\tanh((r - \tilde{R}_{\mathrm{S}})/\Delta_{\mathrm{DW}})) + \arcsin(\tanh((r + \tilde{R}_{\mathrm{S}})/\Delta_{\mathrm{DW}}))\right) \\
&= \frac{4 m_{z,\mathrm{B}} \sinh\left(\frac{r}{\Delta_{\mathrm{DW}}}\right)^2}{\cosh\left(\frac{2r}{\Delta_{\mathrm{DW}}}\right) + \cosh\left(\frac{2\tilde{R}_{\mathrm{S}}}{\Delta_{\mathrm{DW}}}\right)} - m_{z,\mathrm{B}} \\
\text{with} \quad \tilde{R}_{\mathrm{S}} &= \frac{\Delta_{\mathrm{DW}}}{2} \operatorname{arccosh}\left(\cosh\left(\frac{2R_{\mathrm{S}}}{\Delta}\right) - 2\right)
\end{aligned} \tag{S44}$$

where R_{S} is the skyrmion radius defined such that $m_z(R_{\mathrm{S}}) = 0$, $\tilde{R}_{\mathrm{S}}$ is the reparameterized skyrmion radius with $\lim_{\Delta_{\mathrm{DW}} \to 0} \tilde{R}_{\mathrm{S}} = R_{\mathrm{S}}$, Δ_{DW} is the domain-wall width, and $m_{z,\mathrm{B}} = \pm 1$ denotes the background magnetization. Given the relationship between R_{S} and $\tilde{R}_{\mathrm{S}}$, for a given R_{S} (defined by $m_z(R_{\mathrm{S}}) = 0$),

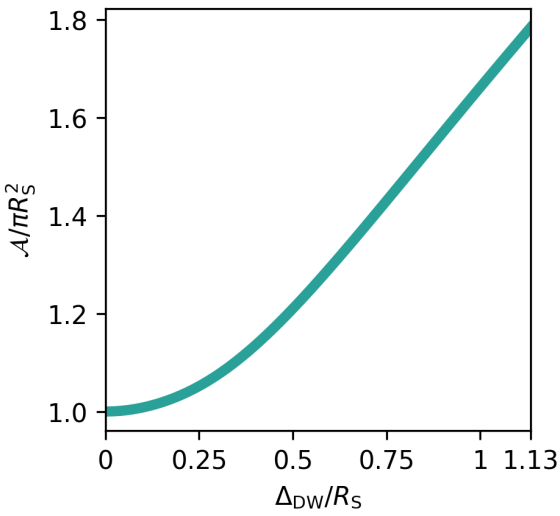

Figure S1: Relationship of the effective area parameter $\mathcal{A}$ to the domain-wall width Δ_{DW} and the skyrmion radius R_{S}, expressed as the dimensionless function $\mathcal{A}(\Delta_{\mathrm{DW}}/R_{\mathrm{S}})/(\pi R_{\mathrm{S}}^2)$. This relationship holds for both small and large skyrmions, as well as for Bloch and Néel skyrmions. Note that for a given skyrmion radius R_{S}, the domain-wall width can only be in the range $0 \leq \Delta_{\mathrm{DW}} \leq 2R_{\mathrm{S}}/\mathrm{arccosh}(3) \approx 1.13\,R_{\mathrm{S}}$ for the skyrmion configuration used here. Note that $\mathcal{A}/\pi R_{\mathrm{s}}^2$ increases with increasing domain wall width Δ_{DW} with fixed skyrmion radius R_{S} because the magnetisation ansatz $m_z(r)$ differs from the background magnetisation for radii larger than R_{s}. Moreover, $m_z(r)$ is not antisymmetric around $r = R_{\mathrm{s}}$, and $m_z(r)$ is weighted by r in the integral. All these factors combined lead to an increase in $\mathcal{A}$.

the domain-wall width can only be in the range $0 \leq \Delta_{\mathrm{DW}} \leq 2R_{\mathrm{S}}/\mathrm{arccosh}(3) \approx 1.13\,R_{\mathrm{S}}$. Note that this parametrization can describe both small and large skyrmions, as well as Bloch and Néel skyrmions.

Using this profile, the effective area parameter $\mathcal{A}$ can be evaluated as

$$\mathcal{A} = -\frac{\pi}{\tanh\left(\tilde{R}_{\mathrm{S}}/\Delta_{\mathrm{DW}}\right)}\left(\frac{\pi^2}{12}\Delta_{\mathrm{DW}}^2 + \tilde{R}_{\mathrm{S}}^2 + \Delta_{\mathrm{DW}}^2 \mathrm{Li}_2\left(-\exp\left(\frac{2\tilde{R}_S}{\Delta_{\mathrm{DW}}}\right)\right)\right), \tag{S45}$$

where $\mathrm{Li}_2(x) = -\int_0^x \mathrm{d}t\, \frac{\log(1-t)}{t}$ denotes the polylogarithm function of order two. The quantity $\mathcal{A}$ satisfies $\mathcal{A} > 0$ and $\lim_{\Delta_{\mathrm{DW}}\to 0} \mathcal{A} = \pi R_{\mathrm{S}}^2$. Furthermore, to understand the behavior of $\mathcal{A}$ for all skyrmions described by the ansatz in Equation S44, the dimensionless effective area parameter $\mathcal{A}(\Delta_{\mathrm{DW}}/R_{\mathrm{S}})$ is plotted in units of πR_{S}^2 in Figure S1.

With this expression for $\mathcal{A}$ and using Equation S42, the AHE signal for a skyrmion including a finite domain-wall width is therefore obtained. For the case where the skyrmion is located at the center of the racetrack ($y_{\mathrm{S}} = 0$) and the potential is measured at $x = 0$, $R_{xy}(x)$ from Equation S42 simplifies to

$$R_{xy}(x_{\mathrm{S}}) = \frac{\rho_{xy}}{t} m_{z,\mathrm{B}}\left(1 - \frac{2}{W^2}\frac{\mathcal{A}}{\cosh\left(\frac{\pi x_{\mathrm{S}}}{W}\right)}\right). \tag{S46}$$

The peak signal, defined as $\Delta R_{xy} = \max_{x_{\mathrm{S}}}(R_{xy}) - \min_{x_{\mathrm{S}}}(R_{xy})$, is then given by

$$\Delta R_{xy} = 2\frac{\rho_{xy}}{t}\frac{\mathcal{A}}{W^2}. \tag{S47}$$

From Figure S1 and Equation S47, the scalability of the approach from micrometer- to nanometer-sized skyrmions follows directly. Note that in the limiting case where the skyrmion reaches its maximum possible size, i.e., $2R_{\mathrm{S}} = W$, and the domain wall can be neglected, i.e., $\Delta_{\mathrm{DW}} = 0$, the result becomes

$$\Delta R_{xy} = \frac{\rho_{xy}}{t}\frac{\pi}{2} \approx \frac{\rho_{xy}}{t} 1.57, \tag{S48}$$

which is smaller than the theoretical maximum value of $2\rho_{xy}/t$.

1.2.4 Domains that vary only along the racetrack

To verify the result for $2R_\mathrm{S} = W$ obtained for skyrmions, and since within this formalism the AHE signal can also be calculated for one-dimensional magnetic domain structures, a direct comparison with the skyrmion case is possible. In this case, the domain-wall profile is described by $m_z(x)$ and is assumed to be independent of y. The domains are embedded in a ferromagnetic background with magnetization $m_{z,\mathrm{B}}$, while the magnetization in the core of the domains is $-m_{z,\mathrm{B}}$. From Equation S11 it follows directly that the particular solution vanishes, i.e., $\phi_{1,\mathrm{p}} = 0$. Furthermore, from Equation S16 one obtains $B_{+W/2}(x) = B_{-W/2}(x) = j\rho_{xx}\left[m_z(x) - m_{z,\mathrm{B}}\right]$. Using Equation S21, Equation S20, the convolution theorem, and the identity $\int_{-\infty}^{\infty} \mathrm{d}k\, \tanh\left(kW/2\right) \exp(ikx)/k = 2\log(\coth(\pi|x|/2W))$ it follows that

$$\begin{aligned} R_{xy} &= \frac{\rho_{xy}}{t}\left[m_{z,\mathrm{B}} + \frac{2}{W}\int_{-\infty}^{\infty} \mathrm{d}k\, \hat{m}_z(k)\frac{1}{k}\tanh\left(\frac{kW}{2}\right)\exp(ikx)\right] \quad \text{with} \quad \hat{m}_z(k) = \frac{1}{2\pi}\int_{-\infty}^{\infty}\left(m_z(x) - m_{z,\mathrm{B}}\right)\exp(-ikx) \\ &= \frac{\rho_{xy}}{t}\left[m_{z,\mathrm{B}} + \frac{2}{\pi W}\int_{-\infty}^{\infty} \mathrm{d}x'\left(m_z(x') - m_{z,\mathrm{B}}\right)\log\left(\coth\left(\frac{\pi}{2W}|x - x'|\right)\right)\right]. \end{aligned} \tag{S49}$$

where both expressions are identical, differing only in the method used to calculate the signal. In the particularly relevant case of a single domain,

$$m_z(x) = \begin{cases} -m_{z,\mathrm{B}}, & |x - x_0| \leq l/2, \\ m_{z,\mathrm{B}}, & |x - x_0| > l/2, \end{cases} \tag{S50}$$

with width l and centered at position x_0. The corresponding AHE signal is then given by

$$\begin{aligned} F(X) &= -\frac{4}{\pi^2}\frac{X}{|X|}\left(2\pi|X|\log(\coth(\pi|X|)) + \mathrm{Li}_2(\tanh(\pi|X|)) - \mathrm{Li}_2(-\tanh(\pi|X|))\right) \\ R_{xy}(x_0) &= \frac{\rho_{xy}}{t} m_{z,\mathrm{B}}\left[1 + F\left(\frac{x_0 + \frac{l}{2} - x}{2W}\right) - F\left(\frac{x_0 - \frac{l}{2} - x}{2W}\right)\right]. \end{aligned} \tag{S51}$$

The peak height is given by

$$\Delta R_{xy} = \max_{x_0}(R_{xy}) - \min_{x_0}(R_{xy}) = \frac{\rho_{xy}}{t}\frac{4}{\pi^2}\left(4\,\mathrm{Li}_2\left(\tanh\left(\frac{l\pi}{4W}\right)\right) - \mathrm{Li}_2\left(\tanh^2\left(\frac{l\pi}{4W}\right)\right) + \pi\frac{l}{W}\log\left(\coth\left(\frac{\pi l}{4W}\right)\right)\right). \tag{S52}$$

It follows directly that $\lim_{l\to\infty} \Delta R_{xy} = 2\rho_{xy}/t$ and $\lim_{l\to 0} \Delta R_{xy} = 0$. For the case where the domain length equals the racetrack width ($l = W$), the peak height becomes

$$\Delta R_{xy} = \frac{\rho_{xy}}{t}\frac{4}{\pi^2}\left(4\,\mathrm{Li}_2\left(\tanh\left(\frac{\pi}{4}\right)\right) - \mathrm{Li}_2\left(\tanh^2\left(\frac{\pi}{4}\right)\right) - \pi\log\left(\tanh\left(\frac{\pi}{4}\right)\right)\right) \approx \frac{\rho_{xy}}{t}1.66. \tag{S53}$$

The maximal signal of $2\rho_{xy}/t$ is therefore not reached for $l = W$, but only in the limit $l \to \infty$, i.e., when the domain width is much larger than the racetrack (or channel) width W. This case has a similar value and validates the result obtained for the skyrmion configuration with $R/2 = W$; see Equation S48.

1.2.5 Finite Hall bar contacts

To conclude with the analytic formulation, finite Hall bar contacts of width W_H located at $x = 0$ are considered. This leads to an extension of the previously defined rectangular domain of width W and length L, resulting in a cross-shaped geometry:

$$\Omega = \left\{(x,y) \in \mathbb{R}^2 \middle| -L/2 \leq x \leq L/2, -W/2 \leq y \leq W/2\right\} \cup \left\{(x,y) \in \mathbb{R}^2 \middle| -W_\mathrm{H}/2 \leq x \leq W_\mathrm{H}/2, -L_\mathrm{H}/2 \leq y \leq L_\mathrm{H}/2\right\} \tag{S54}$$

where L_H denotes the length of the Hall bar contacts, and the limit $L_\mathrm{H} \to \infty$ is considered. The AHE signal is then given by $R_{xy} = (\varphi(x = 0, L_\mathrm{H}/2) - \varphi(x = 0, -L_\mathrm{H}/2))/jWt$. In the following, the cases $W_\mathrm{H} \ll W$ and $W_\mathrm{H} \gg W$ are considered, since solving the current density for the cross geometry is very complicated, particularly in the presence of inhomogeneities induced by the skyrmion.

In the case of $W_\mathrm{H} \ll W$, the Hall contacts do not significantly alter the electrical potential ϕ, as their width is small. Thus, it can be approximated that

$$R_{xy}(x_\mathrm{S}, y_\mathrm{S}, W_\mathrm{H} \ll W) \approx R_{xy}(x_\mathrm{S}, y_\mathrm{S}, W_\mathrm{H} = 0). \tag{S55}$$

A further approximation assumes that the Hall contacts average the electrical potential along the x-direction. For the AHE skyrmion peak height at the center of the racetrack $y_\mathrm{S} = 0$ and at the Hall contact position $x = 0$, this yields from Equation S46

$$\Delta R_{xy}(W_\mathrm{H} \ll W) = \frac{1}{W_\mathrm{H}} \int_{-W_\mathrm{H}/2}^{W_\mathrm{H}/2} \mathrm{d}x \left| m_{z,\mathrm{B}} \frac{\rho_{xy}}{t} - R_{xy}(x) \right| = \frac{\rho_{xy}}{t} \frac{8}{\pi} \frac{\mathcal{A}}{W\, W_\mathrm{H}} \arctan\left[\tanh\left(\frac{\pi}{4} \frac{W_\mathrm{H}}{W} \right) \right], \tag{S56}$$

with $\lim_{W_\mathrm{H} \to 0} \Delta R_{xy} = \frac{\rho_{xy}}{t} \frac{2\mathcal{A}}{W^2}$ which indicates a decrease of ΔR_{xy} for increasing W_H/W.

To analyze the case where the Hall contact has a much larger width than the racetrack width $W_\mathrm{H} \gg W$, the AHE skyrmion peak height signal is again considered for a skyrmion located at the center of the structure. The corresponding rectangular geometry is defined as

$$\Omega = \left\{ (x, y) \in \mathbb{R}^2 \,\middle|\, -W_\mathrm{H}/2 \leq x \leq W_\mathrm{H}/2,\ -L_\mathrm{H}/2 \leq y \leq L_\mathrm{H}/2 \right\}, \tag{S57}$$

with the boundary conditions

$$-\left(\boldsymbol{\rho}^{-1} \nabla\varphi \big|_{x=\pm W_\mathrm{H}/2} \right) \cdot \vec{e}_x = \begin{cases} j, & \text{if } |y| \leq W/2, \\ 0, & \text{otherwise,} \end{cases} \quad \text{and} \quad \left(\boldsymbol{\rho}^{-1} \nabla\varphi \big|_{y=\pm L_\mathrm{H}/2} \right) \cdot \vec{e}_y = 0. \tag{S58}$$

Thus, the current is injected only around the center ($y = 0$) with a width W. This setup corresponds to the Hall cross geometry described in Equation S54, with the approximation that the current density equals $j\,\vec{e}_x$ along the boundaries at $x = \pm W_\mathrm{H}/2$, which is a reasonable assumption for $W_\mathrm{H} \gg W$.

Solving this case follows a similar procedure as in the previous one, allowing the reuse of several intermediate results. The solution can again be expressed as $\varphi = \phi_0 + \theta\,\phi_1$. First, consider the boundary conditions from Equation S58, which simplify to

$$\partial_x(\phi_0 + \theta\,\phi_1) - \theta m_z \partial_y(\phi_0 + \theta\,\phi_1) = \begin{cases} -j\rho_{xx}, & \text{if } |y| \leq W/2, \\ 0, & \text{otherwise,} \end{cases} \quad \theta m_z \partial_x(\phi_0 + \theta\,\phi_1) + \partial_y(\phi_0 + \theta\,\phi_1) = 0 \tag{S59}$$

and lead to a comparison of the coefficients of order θ, neglecting terms of order θ^2, while taking into account that on the boundary $m_z = m_{z,\mathrm{B}}$,

$$\begin{aligned} \partial_x\phi_0|_{x=\pm W_\mathrm{H}/2} &= \begin{cases} -j\rho_{xx}, & \text{if } |y| \leq W/2, \\ 0, & \text{otherwise,} \end{cases} & \partial_y\phi_0|_{y=\pm L_\mathrm{H}/2} &= 0, \\ \partial_x\phi_1|_{x=\pm W_\mathrm{H}/2} &= m_{z,\mathrm{B}} \partial_y\phi_0, & \partial_y\phi_1|_{y=\pm L_\mathrm{H}/2} &= -m_{z,\mathrm{B}} \partial_x\phi_0. \end{aligned} \tag{S60}$$

The first differential equation to be solved is $\Delta\phi_1 = 0$, where the particular solution vanishes. The homogeneous solution is analogous to the previously obtained expression for $\phi_{1,\mathrm{h}}$ and, in the limit $L_\mathrm{H} \to \infty$, is given by

$$\phi_0(x, y) = -\frac{j\rho_{xx}}{\pi} \int_{-\infty}^{\infty} \mathrm{d}k\, \frac{\sinh(kx) \sin\left(\frac{kW}{2}\right)}{\cosh\left(\frac{kW_\mathrm{H}}{2}\right)} \frac{\exp(iky)}{k^2}, \tag{S61}$$

with

$$\partial_x\phi_0|_{x=\pm W_\mathrm{H}}(y) = -\frac{j\rho_{xx}}{\pi} \int_{-\infty}^{\infty} \mathrm{d}k\, \sin\left(\frac{kW}{2}\right) \frac{\exp(iky)}{k} = \begin{cases} -j\rho_{xx}, & \text{if } |y| \leq W/2, \\ 0, & \text{otherwise,} \end{cases} \tag{S62}$$

and $\partial_y\phi_0|_{y\to\pm\infty} = 0$. Therefore, the boundary conditions in Equation S60 are satisfied. The derivatives $\partial_x\phi_0$ and $\partial_y\phi_0$ can be evaluated explicitly using the residue theorem for all (x, y). For the center position $x = 0$, $y = 0$, the result simplifies to

$$j_{\mathrm{c},x} = -\rho_{xx}^{-1}\, \partial_x\phi_0|_{(x,y)=(0,0)} = j\frac{4}{\pi} \arctan\left(\tanh\left(\frac{\pi}{4} \frac{W}{W_\mathrm{H}} \right) \right) \quad \text{and} \quad j_{\mathrm{c},y} = -\rho_{xx}^{-1}\, \partial_y\phi_0|_{(x,y)=(0,0)} = 0. \tag{S63}$$

The current density at the center is therefore given by $\vec{j} = j_{\mathrm{c},x}\,\vec{e}_x$, where $\lim_{W\to\infty} j_{\mathrm{c},x} = j$. For finite W, the current density is reduced compared to j (i.e., $|j_{\mathrm{c},x}| < |j|$) due to the geometric shunting effect.

Based on this, ϕ_1 can be determined from the equation $\Delta\phi_1 = \partial_x m_z\,\partial_y\phi_0 - \partial_y m_z\,\partial_x\phi_0$, together with the boundary conditions mentioned above. The particular solution is given by Equation S11; however, since $\partial_x\phi_0$ depends on both x and y, the corresponding integral becomes complicated. To simplify the problem, it is assumed that within the skyrmion region–where m_z deviates significantly from $m_{z,\mathrm{B}}$–the electrical potential ϕ_0 varies linearly. For the case of the skyrmion AHE peak height signal at the center, this yields, according to Equation S63, $\phi_0 = -j_{\mathrm{c},x}\,\rho_{xx}\,x$. In this case, the particular solution for a skyrmion without domain wall width is given by Equation S26, where j is replaced by $j_{\mathrm{c},x}$, leading to

$$\phi_{1,\mathrm{p}}(x,y) = -\frac{m_{z,\mathrm{B}} - m_{z,\mathrm{S}}}{2} j_{\mathrm{c},x}\rho_{xx} y \begin{cases} 1, & \text{if } x^2+y^2 < R_{\mathrm{S}}^2, \\ \frac{R_{\mathrm{S}}^2}{x^2+y^2}, & \text{otherwise.} \end{cases} \tag{S64}$$

The electrical potential difference of $\phi_{1,\mathrm{p}}$ required to determine R_{xy} is then

$$\lim_{L_{\mathrm{H}}\to\infty} \phi_{1,\mathrm{p}}(0, L_{\mathrm{H}}/2) - \phi_{1,\mathrm{p}}(0, -L_{\mathrm{H}}/2) = 0. \tag{S65}$$

Based on this, the homogeneous solution $\phi_{1,\mathrm{h}}$ can be determined while also taking into account the boundary conditions in Equation S60. The calculation of $\phi_{1,\mathrm{h}}$ follows a similar procedure as in the previous case, leading to the solution

$$\phi_{1,\mathrm{h}} = \int_{-\infty}^{\infty} \mathrm{d}k\, \frac{\hat{B}_{+W_{\mathrm{H}}/2}(k)\cosh\left(k\left(\frac{W_{\mathrm{H}}}{2}+x\right)\right) - \hat{B}_{-W_{\mathrm{H}}/2}\cosh\left(k\left(\frac{W_{\mathrm{H}}}{2}-x\right)\right)}{\sinh(kW_{\mathrm{H}})} \frac{\exp(iky)}{k}, \tag{S66}$$

with the boundary conditions $\hat{B}_{\pm W_{\mathrm{H}}}(k) = \frac{1}{2\pi}\int_{-\infty}^{\infty}\mathrm{d}y\,(\partial_x\phi_{1,\mathrm{h}}|_{x=\pm W_{\mathrm{H}}/2}(y))\exp(-iky)$. Thus, $\phi_1 = \phi_{1,\mathrm{p}} + \phi_{1,\mathrm{h}}$ satisfies the boundary condition in Equation S60, leading to

$$\partial_x\phi_{1,\mathrm{h}}|_{x=\pm W_{\mathrm{H}}/2}(y) = -\,\partial_x\phi_{1,\mathrm{p}}|_{x=\pm W_{\mathrm{H}}/2}(y) + m_{z,\mathrm{B}}\partial_y\phi_0|_{x=\pm W_{\mathrm{H}}/2}(y), \tag{S67}$$

with

$$-\,\partial_x\phi_{1,\mathrm{p}}|_{x=\pm W_{\mathrm{H}}/2}(y) = -j_{\mathrm{c},x}\rho_{xx}R_{\mathrm{S}}^2(m_{z,\mathrm{B}} - m_{z,\mathrm{S}})\frac{(\pm W_{\mathrm{H}}/2)\,y}{((W_{\mathrm{H}}/2)^2+y^2)^2}. \tag{S68}$$

Hence, $\hat{B}_{\pm W_{\mathrm{H}}/2}(k)$ is given by

$$\hat{B}_{\pm W_{\mathrm{H}}/2}(k) = \mp i\frac{jm_{z,\mathrm{B}}\rho_{xx}}{\pi}\tanh\left(k\frac{\mathrm{W_H}}{2}\right)\sin\left(\frac{kW}{2}\right)\frac{1}{k} \pm j_{\mathrm{c},x}\rho_{xx}R_{\mathrm{S}}^2(m_{z,\mathrm{B}} - m_{z,\mathrm{S}})\frac{ik}{4}\exp\left(-\frac{1}{2}|k|W_{\mathrm{H}}\right) \tag{S69}$$

and the homogeneous solution simplifies to

$$\phi_{1,\mathrm{h}}(x,y) = \int_{-\infty}^{\infty}\mathrm{d}k\,\hat{B}_{W_{\mathrm{H}}/2}(k)\frac{\cosh(kx)}{\sinh(kW_{\mathrm{H}}/2)}\frac{\exp(iky)}{k}. \tag{S70}$$

The potential difference $\phi_{1,\mathrm{h}}(0, L_{\mathrm{H}}/2) - \phi_{1,\mathrm{h}}(0, -L_{\mathrm{H}}/2)$, in the limit $L_{\mathrm{H}} \to \infty$, can be simplified by applying the substitution $u = kL_{\mathrm{H}}$. Taking the limit $L_{\mathrm{H}} \to \infty$ and using the integral identity $\int_{-\infty}^{\infty}\mathrm{d}u\,\frac{\sin(u/2)}{u} = \pi$, yields

$$\lim_{L_{\mathrm{H}}\to\infty}\phi_{1,\mathrm{h}}(0, L_{\mathrm{H}}/2) - \phi_{1,\mathrm{h}}(0, -L_{\mathrm{H}}/2) = \rho_{xx}j\,m_{z,\mathrm{B}}W - (m_{z,\mathrm{B}} - m_{z,\mathrm{S}})\,\rho_{xx}\,j_{\mathrm{c},x}\frac{\pi R_{\mathrm{S}}^2}{W_{\mathrm{H}}}. \tag{S71}$$

The AHE signal for the skyrmion, using $\varphi = \phi_0 + \theta\,\phi_1$ and the current $I_x = j\,W\,t$, is therefore

$$R_{xy} = \lim_{L_{\mathrm{H}}\to\infty}\frac{\varphi(0, L_{\mathrm{H}}/2) - \varphi(0, -L_{\mathrm{H}}/2)}{I_x} = \frac{\rho_{xy}}{t}\left[m_{z,\mathrm{B}} - (m_{z,\mathrm{B}} - m_{z,\mathrm{S}})\,\frac{j_{\mathrm{c},x}}{j}\frac{\pi R_{\mathrm{S}}^2}{W\,W_{\mathrm{H}}}\right]. \tag{S72}$$

Analogous to the previous discussion of a skyrmion with a finite domain-wall width, the result including the domain-wall width is

$$R_{xy} = \frac{\rho_{xy}}{t}\left[m_{z,\mathrm{B}} - (m_{z,\mathrm{B}} - m_{z,\mathrm{S}})\,\frac{j_{\mathrm{c},x}}{j}\frac{\mathcal{A}}{W\,W_{\mathrm{H}}}\right], \tag{S73}$$

where $\mathcal{A}$ is the effective area defined in Equation S45. Since $m_{z,\mathrm{B}}\,\rho_{xy}/t$ represents the background signal, the AHE peak height signal is obtained from Equation S63 as

$$\Delta R_{xy}(W_\mathrm{H} \gg W) = \frac{\rho_{xy}}{t}\frac{j_{\mathrm{c},x}}{j}\frac{2\mathcal{A}}{W\,W_\mathrm{H}} = \frac{\rho_{xy}}{t}\frac{2\mathcal{A}}{W\,W_\mathrm{H}}\left[\frac{4}{\pi}\arctan\left(\tanh\left(\frac{\pi}{4}\frac{W}{W_\mathrm{H}}\right)\right)\right]. \tag{S74}$$

This leads to a decrease in ΔR_{xy} with increasing W_H/W, approaching the limit for $W_\mathrm{H}/W \to \infty$:

$$\Delta R_{xy}(W_\mathrm{H} \gg W) = \frac{\rho_{xy}}{t}\frac{2\mathcal{A}}{W_\mathrm{H}^2}. \tag{S75}$$

It should be noted that the only difference between the approximations for ΔR_{xy} in the cases $W_\mathrm{H} \ll W$ and $W_\mathrm{H} \gg W$ is the exchange of W and W_H. Consequently, the expressions for ΔR_{xy} in Equation S74 and Equation S56 are formally identical under this substitution. This also holds in the limits $W_\mathrm{H}/W \to 0$, where $\Delta R_{xy}(W_\mathrm{H} \ll W) = \frac{\rho_{xy}}{t}\frac{2\mathcal{A}}{W^2}$ (Equation S47), and $W_\mathrm{H}/W \to \infty$, where $\Delta R_{xy}(W_\mathrm{H} \gg W) = \frac{\rho_{xy}}{t}\frac{2\mathcal{A}}{W_\mathrm{H}^2}$ (Equation S75). The validity of the approximations for finite Hall bar contact widths W_H is also verified in the following subsection.

1.3 Numerical simulation

In the numerical calculations, the boundary is represented by a polygon; therefore, the boundary conditions are reduced to

$$-(\boldsymbol{\sigma}\,\nabla\varphi|_{\vec{r}})\cdot\vec{n}_i = j_i \quad \text{for } \vec{r} \in E_i, \tag{S76}$$

where E_i is the i-th boundary edge with outward normal vector $\vec{n}_i$, and j_i denotes the current density component flowing perpendicular to the edge.

To simplify the numerical solution of the problem – particularly for the later determination of the values of the resistivity tensor $\boldsymbol{\rho}$ – we introduce the following rescaling. We define the dimensionless resistivity tensor $\tilde{\boldsymbol{\rho}}$ as

$$\tilde{\boldsymbol{\rho}}(\rho_{yx}/\rho_{xx}) = \boldsymbol{\rho}/\rho_{xx} = \begin{pmatrix} 1 & (\rho_{xy}/\rho_{xx})m_z(\vec{r}) \\ -(\rho_{xy}/\rho_{xx})m_z(\vec{r}) & 1 \end{pmatrix}, \tag{S77}$$

which depends only on the ratio ρ_{yx}/ρ_{xx}. Furthermore, we rescale the electric potential by rescaling the spatial coordinates, such that $\varphi(x,y) = \tilde{\varphi}(x/\delta, y/\delta)\,\rho_{xx}\delta j_c$, with $\delta = 1\,\mu\mathrm{m}$ and j_c a fixed reference value for the current density. As a result, the conductivity tensor becomes $\boldsymbol{\sigma} = \tilde{\boldsymbol{\rho}}^{-1}/\rho_{xx}$, and the partial differential equation equation takes the rescaled form:

$$\nabla\cdot\left(\tilde{\boldsymbol{\rho}}^{-1}\nabla\tilde{\varphi}\right) = 0. \tag{S78}$$

The corresponding Neumann boundary condition becomes:

$$-\left(\tilde{\boldsymbol{\rho}}^{-1}\,\nabla\tilde{\varphi}|_{\vec{r}}\right)\cdot\vec{n}_i = j_i/j_c \quad \text{for } \vec{r} \in E_i. \tag{S79}$$

Thus, the partial differential equation for $\tilde{\varphi}$ must be solved. We apply the finite element method by reformulating the problem in its weak form [4]. The weak formulation employs h as the test function and $\tilde{\varphi}$ as the trial function, making use of Gauss's theorem:

$$0 = \int_\Omega \mathrm{d}^2x\,(\nabla\cdot(\tilde{\boldsymbol{\rho}}^{-1}\nabla\tilde{\varphi}))h = -\sum_i\int_{E_i}\mathrm{d}s\,(j_i/j_c)h - \int_\Omega \mathrm{d}^2x\,(\tilde{\boldsymbol{\rho}}^{-1}\nabla\tilde{\varphi})(\nabla\cdot h), \tag{S80}$$

E_i are the boundary edges that together form the boundary $\partial\Omega$, and Ω denotes the domain enclosed by them.

The geometry defined by the boundary (see next section) was triangulated using Gmsh [5], with higher resolution applied in regions where the current density is more inhomogeneous. To solve the finite element problem, FEniCSx was used and the weak form described above was implemented [6]. The function spaces for the test function h and the trial function $\tilde{\varphi}$ were defined using Lagrange elements of degree 4. For the tensor $\tilde{\boldsymbol{\rho}}^{-1}$, a function space of discontinuous Galerkin elements of degree 0 was employed. Since the problem is invariant under the transformation $\varphi \to \varphi + c$ for any constant $c \in \mathbb{R}$, the resulting null space of the linear system is explicitly passed to the solver.

1.3.1 Verification of the analytical results

To verify these results, analogous to the analytical case, a rectangular geometry with width W and aspect ratio $L/W = 100$ was used. The simulations were performed in units of W. The triangulation was carried out using Gmsh with a characteristic mesh length of $0.02\,W$. The strength of the skyrmion Hall effect was set by the ratio $\rho_{xy}/\rho_{xx} = 0.1$. The magnetic background magnetization was set to $m_{z,\mathrm{B}} = 1$.

For the numerical simulation of the skyrmion AHE signal, the skyrmion magnetization ansatz given in Equation S44 was employed, where the limit $\Delta_{\mathrm{DW}} \to 0$ corresponds to Equation S24. The resulting numerical signals were then compared with the general analytical expression for the skyrmion AHE signal $R_{xy} = (\varphi(0, W/2) - \varphi(0, -W/2))/j\,W\,t$ measured at $x = 0$, Equation S42, for various skyrmion positions $x_{\mathrm{S}}, y_{\mathrm{S}}$, as well as for different skyrmion radii R_{S} and domain-wall widths Δ_{DW}. Note that the limit $\Delta_{\mathrm{DW}} \to 0$ corresponds to the case of a skyrmion with a negligible domain-wall width, i.e., Equation S34. The only variable not varied is x; however, its dependence is directly confirmed by translational invariance and the overall prefactor ρ_{xy}/t, which also follows from Equation S22. The resulting comparison is shown in Figure S2, demonstrating very good agreement.

Furthermore, the case of finite Hall bar contact widths W_{H} was examined using the geometry defined in Equation S54 with $L/W = L_{\mathrm{H}}/W = 25$ and the electric potential difference $R_{xy} = (\varphi(0, L_{\mathrm{H}}/2) - \varphi(0, -L_{\mathrm{H}}/2))/j\,W\,t$ for various skyrmion radii R_{S} and domain-wall widths Δ_{DW}, expressed as ratios of the racetrack width W. The triangulation was generated using Gmsh with a characteristic mesh length of $0.01\,W$ within the area $[-1.5\,W, 1.5\,W] \times [-1.5\,W, 1.5\,W]$, and $0.1\,W$ outside this region. The strength of the skyrmion Hall effect was set by the ratio $\rho_{xy}/\rho_{xx} = 0.1$, and the background magnetization was chosen as $m_{z,\mathrm{B}} = 1$. The numerical results are shown in Figure S3 as a function of the Hall bar width normalized to the racetrack width, W_{H}/W, together with the analytical expressions from Equation S56 for the case $W_{\mathrm{H}} \ll W$ and from Equation S74 for the case $W_{\mathrm{H}} \gg W$. It is evident that in the limits $W_{\mathrm{H}}/W \to 0$ and $W_{\mathrm{H}}/W \to \infty$, the peak height approximations are reasonable. Between these limits, a larger deviation appears, particularly around $W = W_{\mathrm{H}}$.

Additionally, the AHE signal R_{xy} measured at $x = 0$ was validated for the case, briefly discussed earlier, where the magnetization varies only along the length. This case was verified using the same geometry, with $m_{z,\mathrm{B}} = 1$ and $\rho_{xy}/\rho_{xx} = 0.1$. In this case, the parameter l and position x_0 was varied, and the numerical signal was computed and compared with Equation S51. Again, the dependencies on x and ρ_{xy}/t follow directly. The results are presented in Figure S4, confirming the validity of the analytical expressions provided in subsubsection 1.2.1 for cases where the magnetization varies at the boundary.

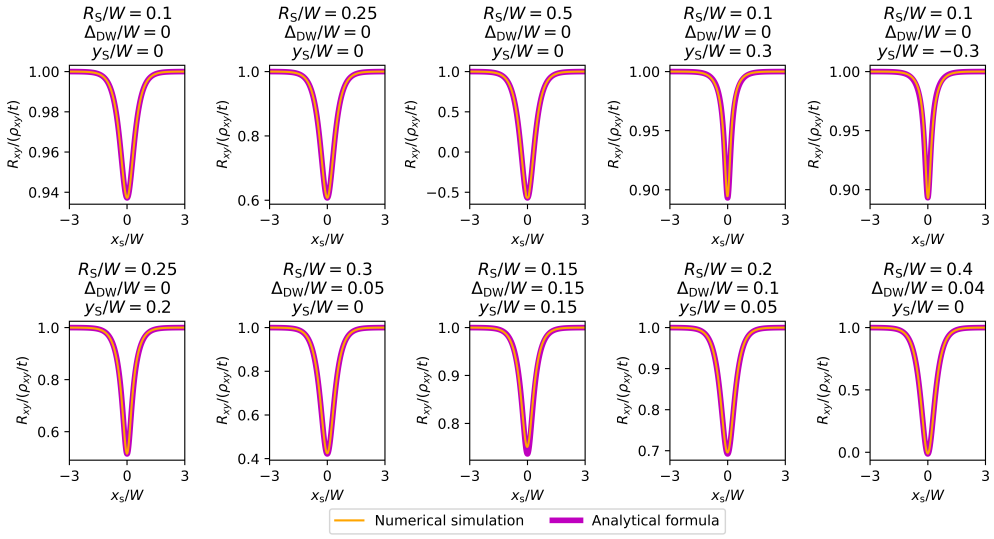

Figure S2: Verification of the analytical formulas Equation S42 and Equation S34 for the AHE signal $R_{xy}(x)$ of a skyrmion, compared with numerical simulations for different ratios R/W, Δ_{DW}/W, and y_{S}/W.

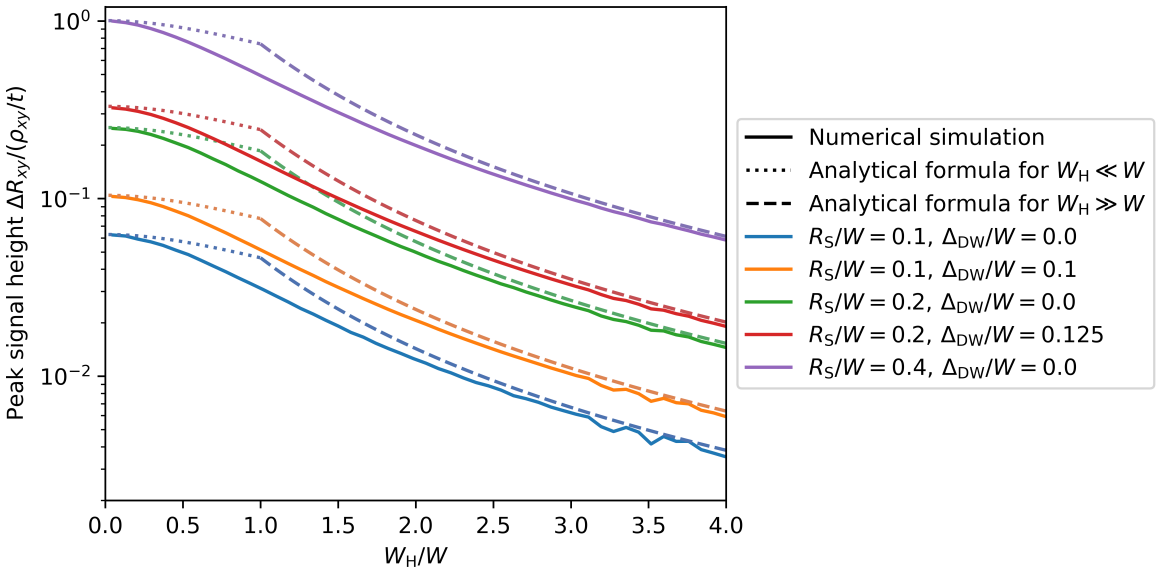

Figure S3: Verification of the analytical formulas in comparison with numerical results for the skyrmion AHE peak height ΔR_{xy} as a function of W_H/W, where W is the racetrack width and W_H is the Hall bar contact width. For the case $W_H \ll W$, Equation S56 is used, while for $W_H \gg W$, Equation S74 is applied.

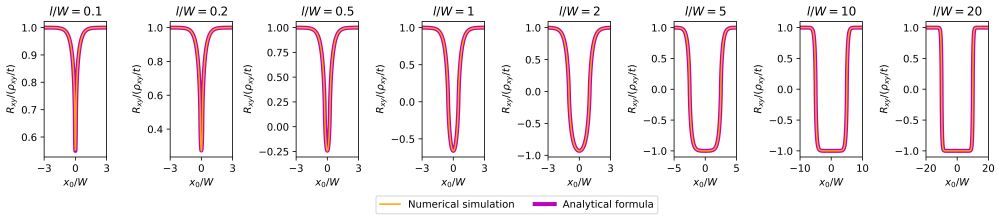

Figure S4: Verification of the analytical formula Equation S51 for the AHE signal $R_{xy}(x)$ of a domain varying only along the length direction, compared with numerical simulations for different lengths l/W.

1.3.2 Geometry

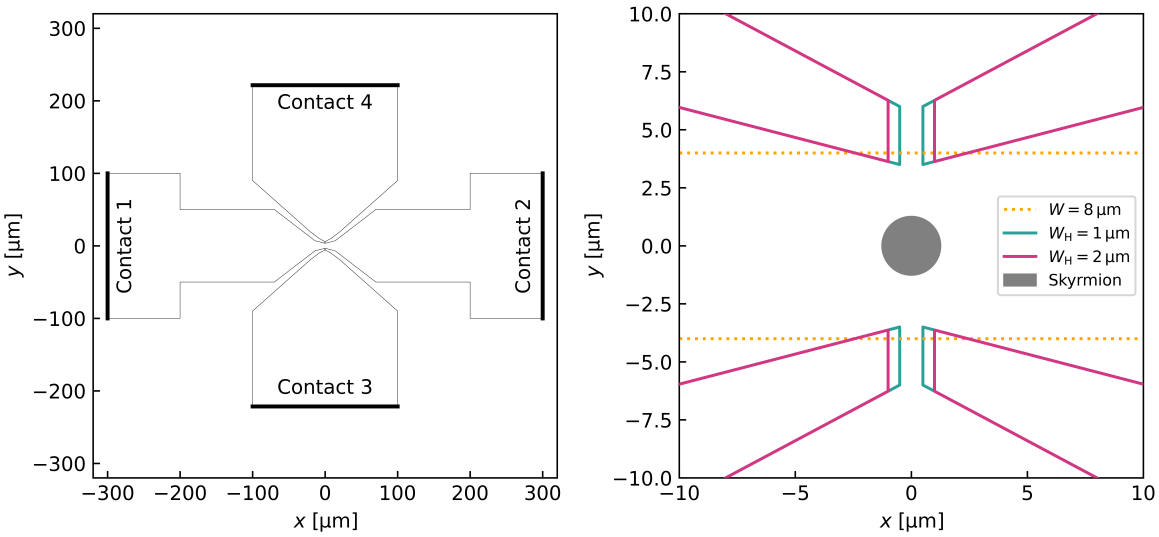

Figure S5: Left: The boundary of the area where current flows with $W_\mathrm{H} = 1\,\mu\mathrm{m}$ for the AHE simulation, similar to the experiment, with the main channel where skyrmions flow and perpendicular Hall contacts. The boundary condition $\vec{j}\cdot\vec{n} \neq 0$ is applied only at the boundary edges of the designated contacts; for all other boundary edges, the condition $\vec{j}\cdot\vec{n} = 0$ holds. Right: A zoomed-in section of the boundary of the geometry in the region where the Hall contact is located. Both versions show the bottleneck of the lateral Hall contacts for $W_\mathrm{H} = 1\,\mu\mathrm{m}$ and $W_\mathrm{H} = 2\,\mu\mathrm{m}$. The two geometries differ only in this region. Additionally, an example skyrmion with $R_\mathrm{S} = 1.25\,\mu\mathrm{m}$ is illustrated, within ρ_{xy} has opposite sign. The skyrmion is shifted along the x-axis in the simulation. The line $W = 8\,\mu\mathrm{m}$ represents the effective width of the channel, which is later used for comparison with the analytical formulas.

The simulations were performed for one and two repetitions of the stack. The total thickness of all conductive layers t is given in Table S1.

For the definition of the geometry used in the AHE simulations, the same CAD geometry as employed in the lithographic fabrication process was used. This geometry is depicted in Figure S5. Due to experimental fabrication tolerances and deviations in the width of the Hall bar contacts, the lateral Hall bar contact width W_H at the bottleneck, which is defined as $W_\mathrm{H} = 1\,\mu\mathrm{m}$ in the lithography CAD file, was also modified to a version with $W_\mathrm{H} = 2\,\mu\mathrm{m}$. Simulations were performed for both values of W_H. The modification affects only the bottleneck region and is shown in Figure S5.

Furthermore, four contacts were defined on the boundary along the edges E_i, which are also indicated in Figure S5. On these boundaries, the normal current density condition $\vec{j}\cdot\vec{n}_i = j_i$ applies, where the index i denotes the contact number from 1 to 4. From current conservation, it follows that $j_2 = -j_1$ and $j_3 = -j_4$. For all other boundary edges E_i, the current density is zero, $j_i = 0$.

During the triangulation process with Gmsh, a characteristic length of $0.05\,\mu\mathrm{m}$ was used in the region $(x, y) \in [-25\,\mu\mathrm{m}, 25\,\mu\mathrm{m}] \times [-10\,\mu\mathrm{m}, 10\,\mu\mathrm{m}]$, and a characteristic length of $5\,\mu\mathrm{m}$ was applied outside this region.

The magnetic background in the simulations is always set to $m_z = -1$. When the anomalous Hall effect is simulated with a skyrmion of radius R_S and position $\vec{r}_\mathrm{S}$ within the defined boundaries, the skyrmion modifies the local m_z value. The estimated skyrmion radius is given in Table S1. We approximate the skyrmion as having a homogeneous magnetization, since the domain wall (DW) width is on the order of $l_\mathrm{DW} = 20\,\mathrm{nm}$ and therefore much smaller. Thus, we model the magnetization as:

$$m_z(\vec{r}) = \begin{cases} 1, & |\vec{r} - \vec{r}_\mathrm{S}| \leq R_\mathrm{S}, \\ -1, & |\vec{r} - \vec{r}_\mathrm{S}| > R_\mathrm{S}. \end{cases} \tag{S81}$$

As a consequence, the resistivity tensor $\boldsymbol{\rho}(x, y)$ is also spatially inhomogeneous, see Equation S1. In the following, voltages U are used, which are defined as differences in the numerically averaged values of the electric potential at the boundary edges E_i:

$$U_{i,j} = \varphi_i - \varphi_j = \rho_{xx}\delta j_c(\tilde{\varphi}_i - \tilde{\varphi}_j), \quad \tilde{\varphi}_i = \frac{1}{l_i}\int_{E_i} \mathrm{d}s\, \tilde{\varphi}(\vec{x}/\delta), \quad l_i = \int_{E_i} \mathrm{d}x\, 1 \tag{S82}$$

where l_i is the edge length. Specifically, we use $U_x = U_{1,2}$ and $U_y = U_{3,4}$. Furthermore, the current I is defined as $I_i = j_i l_i t$. In particular, we use $I_x = I_2$ and $I_y = I_4$. Therefore,

$$R_{i,j,k} = \frac{U_{i,j}}{I_k} = (\tilde{\varphi}_i - \tilde{\varphi}_j)\frac{\rho_{xx}}{t}\frac{\delta}{l}\frac{j_c}{j_k} \tag{S83}$$

with $R_{xx} = R_{1,2,2}$, $R_{yy} = R_{3,4,4}$, and $R_{xy} = R_{3,4,2}$.

Stack	Number of repetitions	t[nm]	R_S[µm]
Ta(4)/$Co_{20}Fe_{60}B_{20}$(0.9)/Ta(0.08)/MgO(2)/HfO(3)	1	4.9	1.25
Ta(4)[Ta(2)/$Co_{20}Fe_{60}B_{20}$(0.9)/Ta(0.04)/MgO(2)]$_2$/HfO(4)	2	9.8	1

Table S1: Properties of the two stacks used for the AHE simulation: Total thickness of all conductive layers t and estimated Skyrmion radius R_S for one and two repetitions.

1.3.3 Determination of the resistivity tensor

For the determination of the resistivity tensor, it follows from Table S1 that the same resistivity tensor $\boldsymbol{\rho}$ can be used for one and two repetitions, since the ratio between the nonmagnetic and magnetic layer thicknesses is identical. To extract the resistivity tensor, ρ_{xx} was determined first. For this purpose, the measured data from Table S2 were used. For both one and two repetitions of the stack, for each corresponding resistance R_{xx} or R_{yy}, and for both widths W, simulations were performed in each case to obtain the potential φ, resulting in a total of eight simulations. The simulation with R_{xx} was performed with $j_1 = -j_2 \neq 0$ and $j_3 = -j_4 = 0$, and ρ_{xx} was then calculated using Equation S83 with $R_{xx} = R_{1,2,2}$. The second simulation with R_{yy} was carried out with $j_1 = -j_2 = 0$ and $j_3 = -j_4 \neq 0$, using $R_{yy} = R_{3,4,4}$, and ρ_{xx} was also calculated using Equation S83. This resulted in a total of 8 values for ρ_{xx}. Averaging these values yields $\rho_{xx} = (156 \pm 26)\,\mu\Omega\,\mathrm{cm}$.

Number of repetitions	R_{xx} [Ω]	R_{yy} [Ω]
1	3561	3571
2	1666	1445

Table S2: Measured values for the determination of longitudinal resistance ρ_{xx}. R_{xx} was measured as the voltage difference between contacts 1 and 2, and R_{yy} as the voltage difference between contacts 3 and 4.

Number of repetitions	$R_{xy}(m_z = 1) - R_{xy}(m_z = 0)$ [Ω]
1	2.5
2	1.25

Table S3: Measured values for the determination of the transverse resistivity ρ_{xy}. The values $R_{xy}(m_z = 1)$ were measured with current applied between contacts 1 and 2, and the voltage measured between contacts 3 and 4. With $R_{xy}(m_z = 0) = 0$.

To calculate ρ_{xy} from the experimental values $R_{xy}(m_z = 1) - R_{xy}(m_z = 0)$ (where m_z is homogeneous) given in Table S3, two equivalent approaches can be used, both yielding the same result. For both one and two repetitions of the stack, with the corresponding resistance R_{xy}, and for both widths W_H, one simulation was performed, resulting in a total of four simulations. Each simulation was carried out with $j_1 = -j_2 \neq 0$ and $j_3 = -j_4 = 0$, and ρ_{xy} was then calculated using Equation S83, with $R_{xy} = R_{3,4,2}$. With $R_{xy}(m_z = 0) = 0$, both theoretically and experimentally. This yielded four values for ρ_{xy}, each of which, within the limits of significant digits, results in $\rho_{xy} = 1.23\,\mu\Omega\,\mathrm{cm}$.

Another approach to determine ρ_{xy} is based on the ideal case of a racetrack without any magnetic texture. Using Equation S22, this leads to the identity $R_{xy} = \rho_{xy}/t$, which results in $\rho_{xy} = 1.23\,\mu\Omega\,\mathrm{cm}$. Both methods – the idealized approach and the one accounting for geometric differences – lead to the same result. The value of ρ_{xy} is of the same order of magnitude as in similar stack [7, 8]. The determined values for the resistivity tensor are also listed in Table S4.

ρ_{xx} [μΩ cm]	ρ_{xy} [μΩ cm]
156	1.23

Table S4: Determined parameters for the resistivity tensor from experiments that are used in the AHE simulation.

1.4 Skyrmion AHE signal results

With the parameters of Table S1 and Table S4, the AHE signal can now be calculated when a skyrmion is present. For this purpose, a current I_x is applied in the x-direction in the main channel, but not in the y-direction ($I_y = 0$), meaning $j_1 = -j_2 \neq 0$ and $j_3 = -j_4 = 0$, i.e., $I_x > 0$. The skyrmion is placed at different positions $\vec{r}_\mathrm{S} = (x_\mathrm{S}, 0)$, and the corresponding $m_z(\vec{r})$ and the resulting resistivity tensor $\boldsymbol{\rho}$ are calculated, from which the electric potential φ is simulated. Using Equation S83, $R_{xy} = R_{3,4,2}$ is calculated. This was done for both Hall bar contact widths W_H, and for both one and two repetitions, with the corresponding skyrmion radius R_S and thickness t. The results are shown in Figure S6, in good agreement with the numerical simulations. The remaining deviation arises from the non-straight geometry of the channel.

In comparison with the simulations, the analytical solution from Equation S46 is used. Since for the experimental skyrmions the domain wall width is much smaller than the radius, i.e., $\Delta_\mathrm{DW} \ll R$, the effective area parameter is given by $\mathcal{A} = \pi R^2$. Note that in the numerical simulations $m_{z,\mathrm{B}} = -1$. However, for the calculation of R_{xy}, the potential difference $\tilde{\varphi}_3 - \tilde{\varphi}_4$ was used, whereas Equation S46 was derived for $\tilde{\varphi}_4 - \tilde{\varphi}_3$. Consequently, when plotting the analytical result for $\tilde{\varphi}_3 - \tilde{\varphi}_4$ with $m_{z,\mathrm{B}} = -1$, two sign inversions occur, leading to the same overall sign. The skyrmion in the simulation is placed at the center of the racetrack; otherwise, Equation S42, which also describes the dependence on y_S, must be used. Because the experimental channel is not perfectly straight, an effective width of $W = 8\,\mu\mathrm{m}$, as shown in Figure S5, is employed. The result obtained using Equation S46 is also presented in Figure S6. The difference between the numerical simulation and the analytical formulas is due to the non-straight experimental channel and the finite lateral Hall bar contact width W_H.

It can be seen that when the skyrmion is far away from the Hall bar contact, the "ideal case" of the resistance for homogeneous magnetization is approached, i.e., the baseline with $R_{xy} = \rho_{xy}/t$, because the presence of the skyrmion no longer plays a significant role. The change in current density due to the skyrmion is so far away that it has no influence on the voltage at the Hall contact bar. When the skyrmion is located near the Hall contact bar, the resulting change in current density is most pronounced, leading to a significant reduction in the transverse resistance R_{xy}. As the skyrmion moves away from this position, the value returns toward the "ideal value" of R_{xy} for the case of a homogeneous magnetization.

In Figure S6, the transverse voltage U_y is also calculated by assuming the same current I_x values as applied in the experiment to measure the AHE signal from a skyrmion. Specifically, $I_x = 10\,\mu\mathrm{A}$ was used for the case of one repetition, and $I_x = 300\,\mu\mathrm{A}$ for two repetitions. From this, the signal height $\Delta R_{xy} = \max(R_{xy}) - \min(R_{xy})$ and $\Delta U_y = I_x \Delta R_{xy}$ was determined, as given in Figure S6. The difference in ΔU_y between the two Hall bar widths, $W_\mathrm{H} = 1\,\mu\mathrm{m}$ and $W_\mathrm{H} = 2\,\mu\mathrm{m}$, is relatively small, with a relative deviation of approximately 10 %. Thus, the exact width of the Hall contact is not a significant factor in this context.

We can also examine how the AHE skyrmion signal peak height, $\Delta U_{xy} = I\,\Delta R_{xy}$, changes as the skyrmion radius varies, in order to estimate how the AHE signal changes with varying skyrmion size. $\Delta R_{xy} = \rho_{xy}/t - R_{xy}(x_\mathrm{S} = 0)$ gives the total peak height of the passing skyrmion in units of resistance. Therefore, $\Delta R_{xy} = \rho_{xy}/t - R_{xy}(x_\mathrm{S})$ is calculated and plotted in Figure S7. For small skyrmion radii R_S, the signal approaches zero, and for larger radii, the signal increases monotonically. Note that the signal also depends on the channel width, which is 8 μm and constant in our calculations.

This dependence of the signal peak maximum on the skyrmion radius also provides the key to a quantitative uncertainty analysis when comparing the simulation and the experiment. The AHE

signal at magnetic saturation, the geometry and thickness of the sample can be precisely measured, and the Hall contact width W_H does not make a significant difference. Therefore, the skyrmion radius within the Hall cross is the dominant uncertainty that significantly influences the AHE peak height. This radius was estimated (see Table S1), but cannot be measured precisely, as the skyrmion moves rapidly through the narrow channel, leading to a smeared appearance due to the finite time resolution. Moreover, its size is likely smaller than that of the static skyrmions outside the channel because of boundary repulsion. The extent to which the skyrmion AHE signal height changes with varying radius, and thus provides the main uncertainity contribution in the simulation and its comparison to the experiment, is shown and plotted in Figure S7. For comparison, the formula for the AHE peak height from Equation S47 is also used, again with $\mathcal{A} = \pi R_\mathrm{S}^2$ and $W = 8\,\mu\mathrm{m}$. The corresponding result is plotted as well in Figure S7, showing good agreement.

The case $W_\mathrm{H} = 1\,\mu\mathrm{m}$, with the parameters for a single repetition (see Table S1), which is plotted in the left panel of Figure S6, corresponds to subfigure 1(c) in the main text. The simulated values for R_{xy}, U_y, and ΔU_y show good agreement with the experimental results. For comparison, Equation S46 is also plotted using $\mathcal{A} = \pi R_\mathrm{S}^2$ and $W = 8\,\mu\mathrm{m}$.

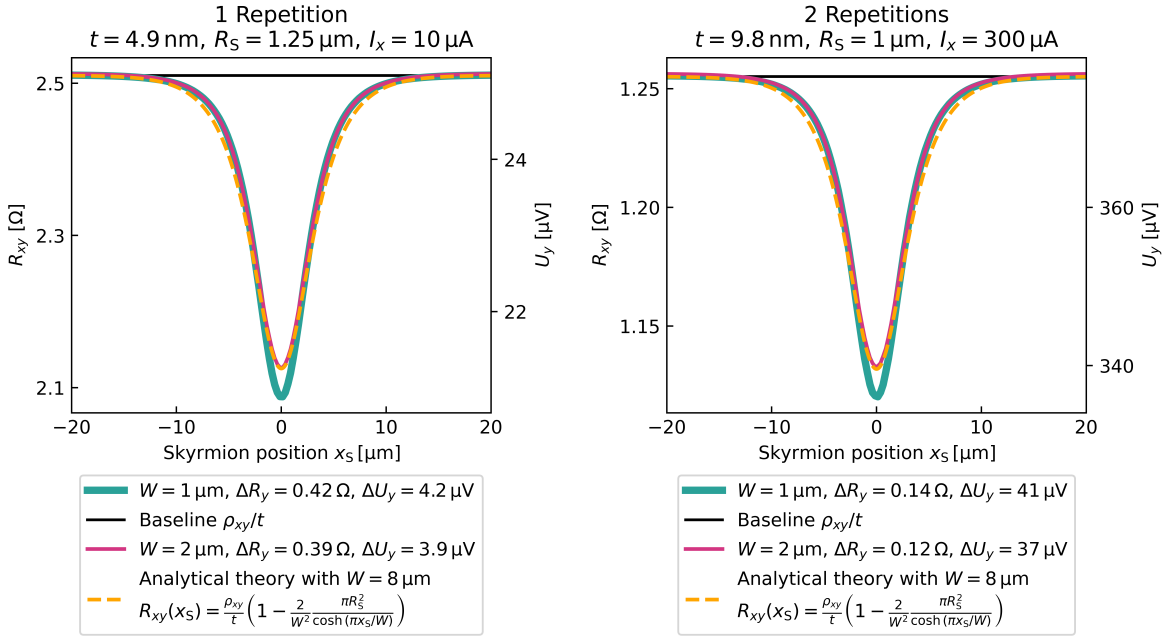

Figure S6: AHE signal for one skyrmion. The transverse resistance R_{xy} is plotted as a function of the skyrmion displacement for a skyrmion of radius R_S. The position is defined such that $y_\mathrm{S} = 0$, and x_S is specified as shown in Figure S5. The plot shows the simulation results together with the analytical expression from Equation S46, using an effective channel width of $W = 8\,\mu\mathrm{m}$. In addition to the transverse resistance R_{xy}, the voltage U_y measured transversely is also shown, assuming a certain longitudinal current I_x is applied. The plots show the signal for different widths of the Hall bar contacts, $W_\mathrm{H} = 1\,\mu\mathrm{m}$ and $W_\mathrm{H} = 2\,\mu\mathrm{m}$. Also indicated in the legend is ΔR_{xy} and ΔU_y, the corresponding signal range is defined as $\Delta R_{xy} = \max(R_{xy}) - \min(R_{xy})$ and $\Delta U_y = I \Delta R_{xy}$. Left: For one repetition of the stack, where the conductive layers have a total thickness of $t = 4.9\,\mathrm{nm}$, the skyrmion has a radius of $R_\mathrm{S} = 1.25\,\mu\mathrm{m}$, and a current of $I_x = 10\,\mu\mathrm{A}$ is applied in the x-direction. Right: For two repetitions of the stack, where the conductive layers have a total thickness of $t = 9.8\,\mathrm{nm}$, the skyrmion has a radius of $R_\mathrm{S} = 1\,\mu\mathrm{m}$, and a current of $I_x = 300\,\mu\mathrm{A}$ is applied in the x-direction. Additionally, a reference line ρ_{xy}/t is included in each plot, representing the expected value in the case of homogeneous magnetization and current density.

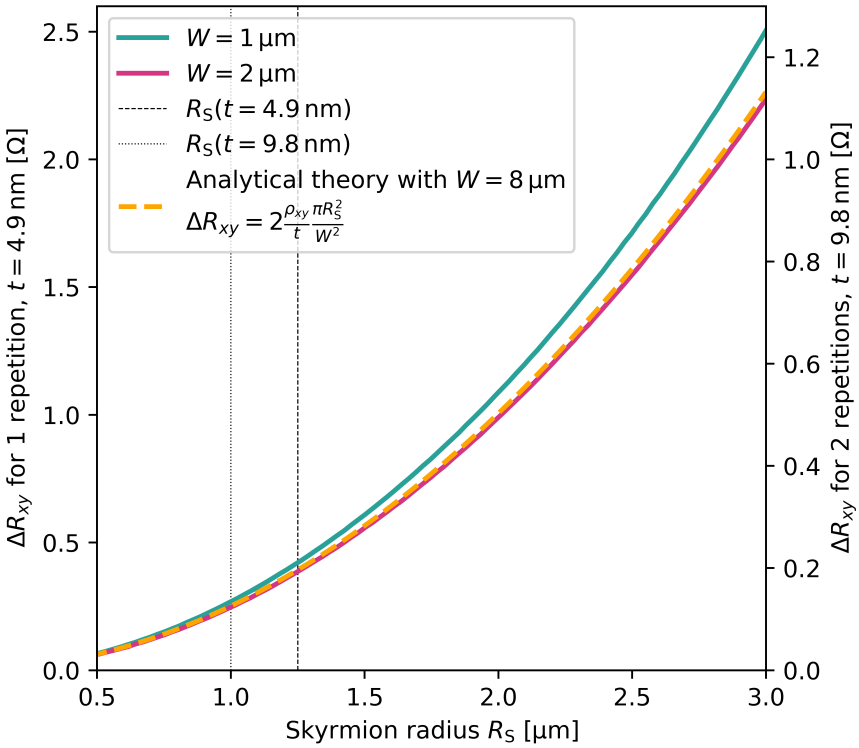

Figure S7: Dependence of the AHE signal peak height ΔR_{xy} on the skyrmion radius R_S. The left y-axis shows the ΔR_{xy} signal for one repetition with $t = 4.9\,nm$, and the right y-axis shows the ΔR_{xy} signal for two repetitions with $t = 9.8\,nm$, where the maximal R_{xy} signal is about half as large due to the scaling $R_{xy} \sim t^{-1}$. The plot presents the simulation results alongside the analytical expression given by Equation S47, assuming an effective channel width of $W = 8\,\mu m$. Also shown as vertical lines are the radii that were estimated for one and two repetitions for the results in Figure S6.

2 Sample Preparation

The multilayer stacks examined in this study were fabricated using a Singulus Rotaris magnetron sputtering system. Perpendicular magnetic anisotropy (PMA) arises in the samples primarily from the interface between MgO and the $Co_{20}Fe_{60}B_{20}$ ferromagnetic layer. A base layer of tantalum (Ta) is incorporated to induce spin-orbit torques into the ferromagnetic layer. Additionally, a thin Ta (0.08 nm) dusting layer positioned between the MgO and $Co_{20}Fe_{60}B_{20}$ tunes the PMA strength and creates a low pinning environment for the magnetic skyrmions. Oxidation is prevented by a hafnia oxide capping layer, leading to a robust multilayer configuration that supports skyrmion formation at temperatures above room temperature, with low pinning effects and high thermal diffusion. The diameter of skyrmions in the system is typically 3 μm to 5 μm, depending on both temperature and the out-of-plane magnetic field.

Patterned device structures were defined via optical lithography, followed by argon ion etching using an IonSys Model 500 ion beam etching system. For skyrmion observation, the experimental setup utilizes a magneto-optical Kerr effect (MOKE) microscope produced by evico magnetics GmbH. The microscope is connected to a CCD camera capturing images at 16 frames per second, with an exposure time of 62.5 ms and a native resolution of 1920 × 1200 pixels. When 2x2 binning is applied, the resolution decreases to 960 × 600 pixels, which increases the signal-to-noise ratio. Enhanced contrast is achieved by computing the differential image between the skyrmion state and the fully saturated magnetic state.

The current injection to the sample is provided by a Keithley 2400 source meter, while Hall voltage measurements are performed using Keithley 2182A nanovolt meters. Longitudinal and transversal resistances of approximately 4 kΩ are exhibited by the devices.

3 Hysteresis

To validate the Hall sensor properties, complete out-of-plane hysteresis loops were performed simultaneously measuring the anomalous Hall voltage and imaging with Kerr microscopy. The resulting signal can be directly correlated with the Kerr intensity measured at the junction, as shown in Figure S8(a). The data shows identical behavior, as expected. The minor differences observed can be attributed to the only approximated region of interest selected for the Kerr imaging analysis. The specific region of interest is illustrated in Figure S8(b).

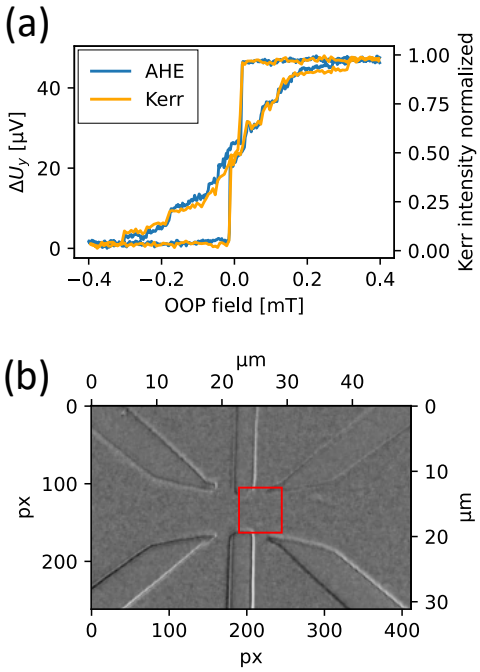

Figure S8: (a) Anomalous Hall Effect (AHE) voltage and Kerr intensity, at out of plane (OOP) field hysteresis. (b) Kerr microscope image of device used in (a). Red rectangle marks region of interest used for Kerr intensity used in (a).

References

[1] Naoto Nagaosa, Jairo Sinova, Shigeki Onoda, A. H. MacDonald, and N. P. Ong. "Anomalous Hall effect". In: *Rev. Mod. Phys.* 82 (2 May 2010), pp. 1539–1592. DOI: 10.1103/RevModPhys.82.1539. URL: https://link.aps.org/doi/10.1103/RevModPhys.82.1539.

[2] Riccardo Hertel and Attila Kákay. "Hybrid finite-element/boundary-element method to calculate Oersted fields". In: *Journal of Magnetism and Magnetic Materials* 369 (2014), pp. 189–196. ISSN: 0304-8853. DOI: https://doi.org/10.1016/j.jmmm.2014.06.047. URL: https://www.sciencedirect.com/science/article/pii/S0304885314005691.

[3] Niklas Romming, André Kubetzka, Christian Hanneken, Kirsten von Bergmann, and Roland Wiesendanger. "Field-Dependent Size and Shape of Single Magnetic Skyrmions". In: *Phys. Rev. Lett.* 114 (17 May 2015), p. 177203. DOI: 10.1103/PhysRevLett.114.177203. URL: https://link.aps.org/doi/10.1103/PhysRevLett.114.177203.

[4] Anders Logg, Kent-Andre Mardal, and Garth Wells. *Automated solution of differential equations by the finite element method: The FEniCS book*. Vol. 84. Springer Science & Business Media, 2012.

[5] Christophe Geuzaine and Jean-François Remacle. "Gmsh: A three-dimensional finite element mesh generator with built-in pre- and post-processing facilities". In: *International Journal for Numerical Methods in Engineering* 79.11 (2009), pp. 1309–1331. DOI: 10.1002/nme.2579.

[6] Igor A. Baratta, Joseph P. Dean, Jørgen S. Dokken, Michal Habera, Jack S. Hale, Chris N. Richardson, Marie E. Rognes, Matthew W. Scroggs, Nathan Sime, and Garth N. Wells. *DOLFINx: the next generation FEniCS problem solving environment*. preprint. 2023. DOI: 10.5281/zenodo.10447666.

[7] Tao Zhu. "Anomalous Hall effect in perpendicular CoFeB thin films". In: *Chinese Physics B* 23.4 (2014), p. 047504.

[8] Davide Maccariello, William Legrand, Nicolas Reyren, Karin Garcia, Karim Bouzehouane, Sophie Collin, Vincent Cros, and Albert Fert. "Electrical detection of single magnetic skyrmions in metallic multilayers at room temperature". In: *Nature Nanotechnology* 13.3 (Mar. 2018), pp. 233–237. ISSN: 1748-3395. DOI: 10.1038/s41565-017-0044-4. URL: https://doi.org/10.1038/s41565-017-0044-4.